



HAL
open science

Dehydration of the Subducting Juan de Fuca Plate and Fluid Pathways Revealed by Full Waveform Inversion of Teleseismic P and SH Waves in Central Oregon

Li-yu Kan, Sébastien Chevrot, Vadim Monteiller

► **To cite this version:**

Li-yu Kan, Sébastien Chevrot, Vadim Monteiller. Dehydration of the Subducting Juan de Fuca Plate and Fluid Pathways Revealed by Full Waveform Inversion of Teleseismic P and SH Waves in Central Oregon. *Journal of Geophysical Research : Solid Earth*, 2023, 128 (4), 10.1029/2022JB025506 . hal-04234561

HAL Id: hal-04234561

<https://hal.science/hal-04234561>

Submitted on 17 Oct 2023

HAL is a multi-disciplinary open access archive for the deposit and dissemination of scientific research documents, whether they are published or not. The documents may come from teaching and research institutions in France or abroad, or from public or private research centers.

L'archive ouverte pluridisciplinaire **HAL**, est destinée au dépôt et à la diffusion de documents scientifiques de niveau recherche, publiés ou non, émanant des établissements d'enseignement et de recherche français ou étrangers, des laboratoires publics ou privés.

JGR Solid Earth

RESEARCH ARTICLE

10.1029/2022JB025506

Key Points:

- We image the structure in density, V_p , V_s , and V_p/V_s of Cascadia subduction zone by inversion of teleseismic P and SH waveforms
- The tomographic model provides evidence for a fluid-saturated subducting Juan de Fuca oceanic crust
- The eclogitization of the oceanic crust starts around 40 km depth and expels water into the forearc mantle wedge

Correspondence to:

S. Chevrot,
sebastien.chevrot@get.omp.eu

Citation:

Kan, L.-Y., Chevrot, S., & Monteiller, V. (2023). Dehydration of the subducting Juan de Fuca plate and fluid pathways revealed by full waveform inversion of teleseismic P and SH waves in central Oregon. *Journal of Geophysical Research: Solid Earth*, 128, e2022JB025506. <https://doi.org/10.1029/2022JB025506>

Received 31 AUG 2022

Accepted 15 MAR 2023

Author Contributions:

Conceptualization: Sébastien Chevrot, Vadim Monteiller

Formal analysis: Li-Yu Kan, Sébastien Chevrot, Vadim Monteiller

Investigation: Li-Yu Kan, Sébastien Chevrot

Methodology: Li-Yu Kan, Sébastien Chevrot, Vadim Monteiller

Resources: Sébastien Chevrot, Vadim Monteiller

Software: Li-Yu Kan, Sébastien Chevrot, Vadim Monteiller

Supervision: Sébastien Chevrot, Vadim Monteiller

Validation: Li-Yu Kan, Vadim Monteiller

Writing – original draft: Li-Yu Kan, Sébastien Chevrot, Vadim Monteiller

Writing – review & editing: Li-Yu Kan, Sébastien Chevrot, Vadim Monteiller

Dehydration of the Subducting Juan de Fuca Plate and Fluid Pathways Revealed by Full Waveform Inversion of Teleseismic P and SH Waves in Central Oregon

Li-Yu Kan¹ , Sébastien Chevrot¹ , and Vadim Monteiller²

¹GET, UMR 5563, Observatoire Midi Pyrénées, Université Paul Sabatier, CNRS, IRD, Toulouse, France, ²Aix Marseille University, CNRS, Centrale Marseille, LMA UMR 7031, Marseille, France

Abstract The dehydration of subducting slabs expels a massive amount of water into the forearc and backarc mantle which is responsible for the serpentinization of the mantle wedge, as well as the production of melt and arc magmatism. These processes are expected to have characteristic signatures in density and seismic velocities models, which remain largely elusive to date due to the limited spatial resolution of classical passive tomographic approaches. Here we present a tomographic model of density, V_p , V_s , and V_p/V_s beneath central Oregon, obtained by inverting complete teleseismic P and SH waveforms recorded by the CASC93 temporary experiment. The final model shows an east-dipping low-velocity layer less than 10 km thick that can be associated with the fluid-saturated Juan de Fuca oceanic crust. The distribution of tremors at the surface closely coincides with the horizontal extent of this low-velocity layer. Below 40 km depth, seismic velocities and density increase progressively to the values of a typical mantle. This transitional domain corresponds to the eclogitization of the oceanic crust. Silica-saturated fluids released by pore collapse migrate upward, producing serpentinization reactions in the forearc mantle that lower the density and seismic velocities. The very low V_p/V_s ratio documented in the Cascadia forearc crust is evidence that these silica-saturated fluids reach the crust, where they produce extensive quartz mineralization. At greater depth, a low seismic velocity and high V_p/V_s ratio anomaly provides evidence for partial melting at around 75 km depth beneath the volcanic arc.

Plain Language Summary The subduction of the hydrated oceanic lithosphere injects large amounts of water into the Earth's interior. However, owing to the limited spatial resolution of classical tomographic approaches, the fluid pathways and related metamorphic reactions remain elusive. In this study, we image the Cascadia subduction beneath central Oregon by inverting complete P and SH teleseismic waveforms. The resulting tomographic models of density and seismic velocities reveal the eclogitization reactions in the subducting Juan de Fuca oceanic crust and the associated release of fluids into the forearc mantle. These silica-saturated fluids migrate upward, producing serpentinization of the forearc mantle. When these fluids reach the crust, the temperature decrease produces quartz mineralization, as evidenced by the very low V_p/V_s ratio observed in the Cascadia forearc crust. At greater depth, we find evidence of partial melting around 75 km depth below the volcanic arc, resulting from dehydration of the slab that lowers the solidus temperature in the lithospheric mantle of the upper plate.

1. Introduction

Subduction of hydrated oceanic lithosphere introduces massive amounts of water into the deep Earth (e.g., S. A. Peacock, 1990). This water controls the mechanical properties of the subduction interface and the depth distribution of earthquakes and episodic tremor and slip (S. M. Peacock & Hyndman, 1999). The temperature-dependent transition from blueschist to eclogite facies governs the dehydration of the subducting plate (S. M. Peacock & Wang, 1999). For example, for the cold and old Pacific plate subducting beneath NE Japan, this transition is around 110 km depth whereas for the hot and young Philippine Sea plate subducting beneath SW Japan, the downgoing oceanic crust enters the eclogite facies at around 50 km depth (S. M. Peacock & Wang, 1999). These estimates are in good agreement with the seismologically constrained depth extent of a low seismic velocity layer often interpreted as the fluid-saturated oceanic crust (e.g., M. Bostock, 2013). The eclogitization of the downgoing oceanic crust and the related collapse of porosity release large amounts of fluids in the upper plate. These silica-saturated fluids will percolate through and transforms the forearc mantle into weak assemblages of serpentine, talc, and brucite (S. M. Peacock & Hyndman, 1999). In warm subduction zones, the downip limit of

subduction earthquakes is thus controlled by the depth at which the subducting slab intersects the forearc mantle (S. M. Peacock & Hyndman, 1999; Oleskevich et al., 1999; Hyndman, 2013; Hyndman et al., 2015). At deeper levels, water released by the dehydrating subducting plate will lower the solidus temperature, triggering the partial melt of mantle material that will migrate upward to feed the volcanic arc (S. A. Peacock, 1990).

Despite the important role played by fluids in arc magmatism and more generally in the processes occurring in subduction zones, fluid transfers and pathways in the mantle wedge and forearc crust remain largely elusive. The motivation of this study is to investigate the potential of full waveform inversion of teleseismic body waves to provide new tomographic constraints on deep subduction processes. In particular, recent methodological development has shown that accounting for the correlation between density and seismic velocities improves very significantly the reconstruction of density and V_p/V_s models (Kan et al., 2023). These two parameters are of special interest because they are reliable indicators of the presence of water, partial melt (e.g., Nakajima et al., 2001; Watanabe, 1993), or serpentinized mantle (Christensen, 2004).

For the first application of our multi-parameter full waveform inversion approach, we focus on Cascadia, which stands among the most well-studied subduction zone worldwide and represents the end member of hot and young subduction, where extensive shallow dehydration of the subducting plate is expected to occur. Fluid processes are thus expected to be strongly expressed in the structural variations of seismic velocities, and in particular of the V_p/V_s ratio.

Along the Cascadia subduction margin, which extends from northern California to southern British Columbia, the Juan de Fuca (JdF) plate underthrusts the northern America plate with a convergence rate that ranges from 30 mm/yr at its southern end and 45 mm/yr in its northern end (Wilson, 1993). In contrast to Northern Cascadia where seismicity is abundant, earthquakes in central Cascadia are scarce, so the geometry of the subducting slab (McCroory et al., 2012) is poorly constrained and tomographic studies rely primarily on seismic recordings of distant teleseismic sources. Regional travel time tomography has found that the fast anomaly associated with the subducting Juan de Fuca plate can be traced down to the transition zone except beneath central Oregon where it disappears around 200 km depth (James et al., 2011; Obrebski et al., 2010, 2011; Schmandt & Humphreys, 2010). The Juan de Fuca is thus fragmented (e.g., Obrebski et al., 2010), and the limited depth extension of the subduction beneath central Oregon which implies a small slab pull force, may explain the lack of deep seismicity in that region.

In Cascadia, as in many other subduction zones, receiver function studies have revealed the presence of a thin (less than 10 km thick) low seismic velocity and high V_p/V_s ratio layer (Audet et al., 2009, 2010; Hansen et al., 2012; M. G. Bostock et al., 2002; M. Bostock, 2013; Tauzin et al., 2016). Episodic tremor and slip have been well studied in Cascadia (Rogers & Dragert, 2003). While tremor locations are poorly constrained, especially for their depths (Wech, 2021; Wech & Creager, 2008), tremors seem to be related to the overpressured oceanic crust, that is, to the thin east-dipping low-velocity layer evidenced by receiver function studies (Audet et al., 2009). The serpentinization of the forearc mantle in Cascadia is now well documented by both geological and geophysical observations (S. M. Peacock, 1993; Hyndman & Peacock, 2003; M. G. Bostock et al., 2002; Blakely et al., 2005). Local earthquake tomography studies in northern Cascadia have documented very low V_p/V_s (lower than 1.7) in the forearc crust (Audet & Bürgmann, 2014; Guo et al., 2021; Ramachandran & Hyndman, 2012; S. M. Peacock et al., 2011; Hyndman et al., 2015; Savard et al., 2018). Such low values can only be explained by a significant quartz enrichment (Chevrot & van der Hilst, 2000). This would suggest that part of the silica-saturated fluids expelled by dehydration of the subduction slab reach the crust where the temperature decrease will produce massive quartz mineralizations. This process may have important consequences for the formation and evolution of a silica-enriched continental crust.

Here, we invert the waveforms of nine teleseismic events recorded by the stations of the CASC93 experiment in order to obtain models of density, V_p , V_s , and V_p/V_s beneath central Oregon, from the surface down to 300 km depth. We first describe the data selection and preparation, and the principles of the inversion method. We then present the results of the inversion and discuss the main features of the final model. Finally, we provide interpretations of the structural anomalies in density, seismic velocities, and V_p/V_s in terms of the different subduction processes that occur at depth as well as comparisons with previous geophysical studies.

2. Data and Methodology

2.1. The CASC93 Experiment

We use P and SH waveform records from the three-component broadband seismometers of the CASC93 temporary experiment, deployed along an E-W transect in central Oregon from March to December 1993 (Nabelek

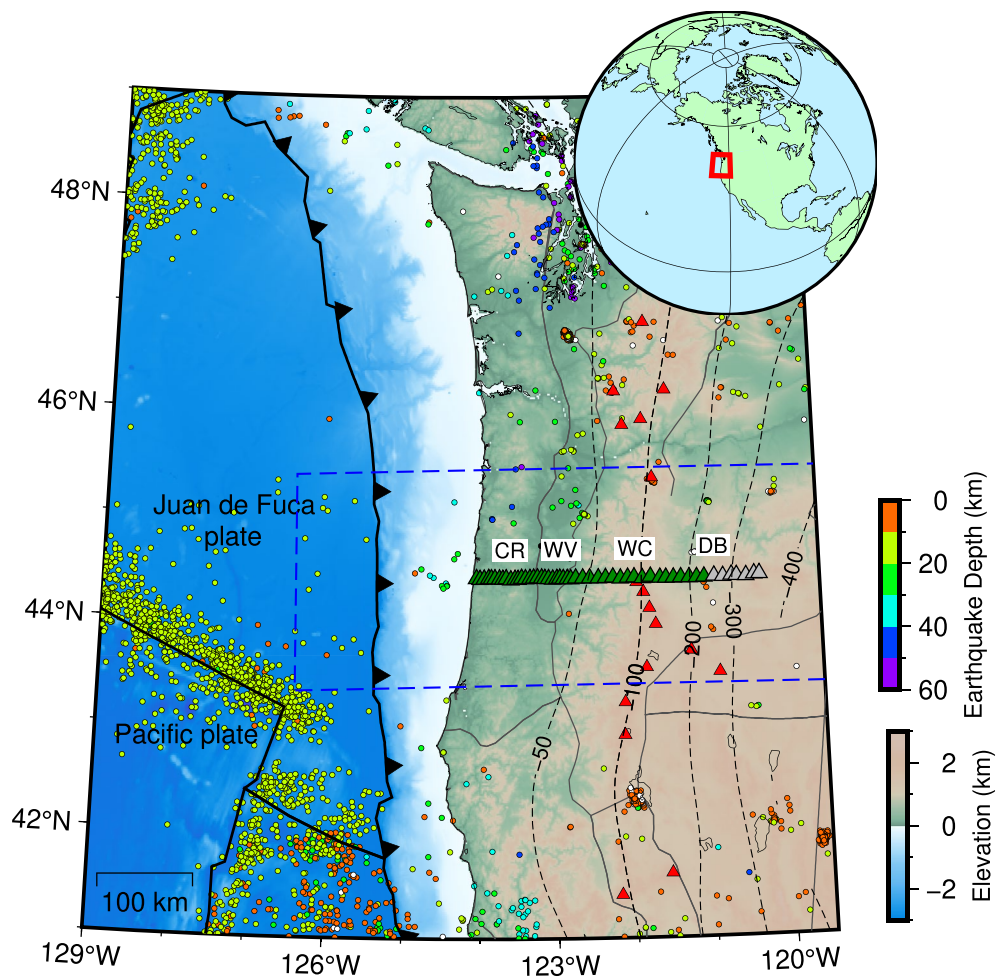


Figure 1. Positions of the CASC93 broadband stations (green triangles) and physiographic provinces of Oregon. The gray triangles show the stations that were discarded owing to the absence of well-recorded teleseismic events. The blue dashed line outlines the inversion domain (Figure 5). The color circles correspond to the $M \geq 3.0$ earthquakes in the USGS catalog from 1990 to 2022. The red triangles show the positions of Holocene volcanoes. The black dashed lines represent the isovalues of slab depth, taken from the Slab2 model (Hayes et al., 2018). CR: Coastal Range, WV: Willamette Valley, WC: Western Cascades, DB: Deschutes Basin.

et al., 1993) (Figure 1). As demonstrated in Beller, Monteiller, Combe, et al. (2018), 2D arrays are always preferable to 1D transects, even if the station distribution is sparser. While other more recent deployments (e.g., the USArray Transportable Array) could provide additional coverage away from the CASC93 line, the lack of overlapping operational times limits their usefulness here. The waveform inversion is performed on a selection of teleseismic events (epicentral distance between 30° and 90°) with magnitude larger than 6 and large signal-to-noise ratio.

2.2. Data Selection and Preparation

Because in FWI we fit complete waveforms, that is, every wiggle observed on the seismic traces within a certain frequency band, the records that enter the inversion need to be carefully selected. Waveform data are first downloaded from the IRIS datacenter (<https://www.iris.edu>). We then apply basic signal processing (i.e., remove mean and trend) before applying a taper and removing the station response on each record. Next, we inspect each event and determine travel time and amplitude residuals at each station. We first determine a reference wavelet by aligning and averaging all the records. The travel time residuals are obtained from the time shifts measured by cross-correlation between the reference wavelet and each individual trace after removing their average. The amplitude residual δA_i for station i is defined as

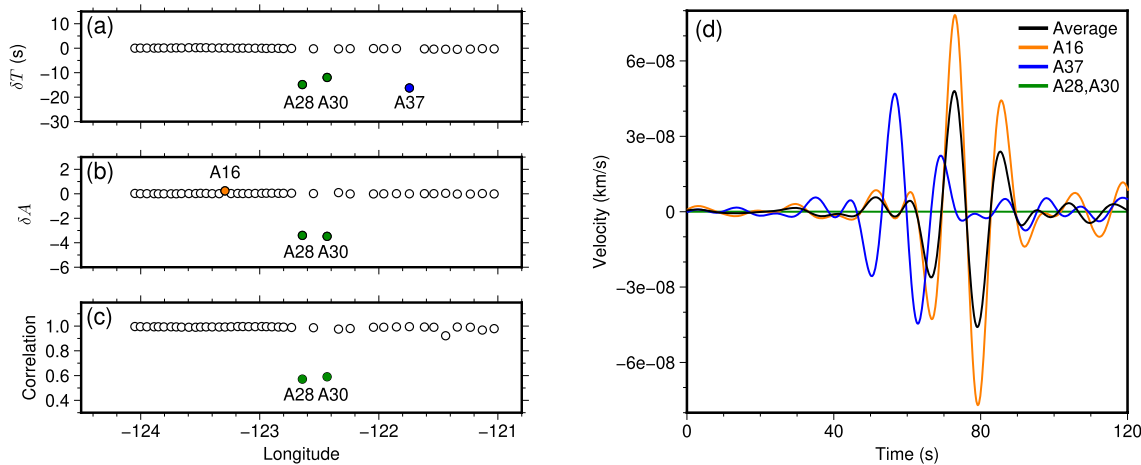


Figure 2. Example of data selection procedure for the vertical component of event 9 in Table 1. (a) Travel time residuals. Negative residuals represent phases arriving earlier than the average trace. (b) Amplitude residuals. (c) Correlation coefficient of each station and the average trace. (d) Observed vertical data filtered between 10 and 25 s period.

$$\delta A_i = \log_{10} \left(\frac{\int_{t_1}^{t_2} |u_i(t)|^2 dt}{\int_{t_1}^{t_2} |\bar{u}(t)|^2 dt} \right). \quad (1)$$

where $u_i(t)$ is the observed trace at station i and $\bar{u}(t)$ is the reference average wavelet. For P waves, these residuals are measured on the vertical component, whereas for SH waves, they are measured on the transverse component. When visualized in map view, the travel time and amplitude residuals allow us to quickly identify stations with abnormal time or amplitude, which are removed from the data set.

The data selection procedure is illustrated with event 9 (Figure 2). The waveforms are filtered between 10 and 25 s periods, which corresponds to the frequency band used in the first inversion. The vertical component of station A28 and A30 is flat, with very small amplitudes compared with those at the other stations. A large negative travel time anomaly is observed at station A37, presumably due to a clock problem (Figure 2a). Finally, the relative amplitude anomaly at station A16 is 0.24, which means the amplitude at this station is 1.6 times larger than at adjacent stations. We thus decided to also remove the records of this station for this particular event.

Owing to the limited duration of the acquisition, we only found 7 P and 4 SH teleseismic arrivals of sufficient quality for FWI at periods down to 4 s (Figure 3). The event information is given in Table 1.

2.2.1. Source Wavelet Estimation

To compute synthetic seismograms of teleseismic body waves we need the apparent incident source wavelet for each selected event. To determine these source wavelets, we first compute the Green's functions for each event that corresponds to a short duration (here 2 s) Gaussian source wavelet (Monteiller et al., 2021). These computations are performed with AxiSEM in the ak135 reference Earth model (Kennett et al., 1995). The source wavelet is then obtained by first deconvolving the Green's function from the observed vertical component at each station, using a simple water-level deconvolution in the frequency domain. The deconvolved traces are then aligned with respect to the first trace and averaged. Finally, the source wavelet is shifted so that the average time residual between synthetic and observed traces is zero. This time correction is necessary to remove the contribution of heterogeneities located outside the tomographic grid, similar to the practices in classical regional travel time tomography (Aki et al., 1977).

2.3. Design of the Tomographic Mesh

We build a spectral-element mesh that represents a chunk of the spherical Earth, centered at -122.2° longitude and 44.4° latitude (Figure 5). The size of the mesh is 6° in longitude and 2° in latitude, with hexahedral elements of about 6 km in size. Surface topography from the ETOPO1 Global Relief Model is applied on the upper edge

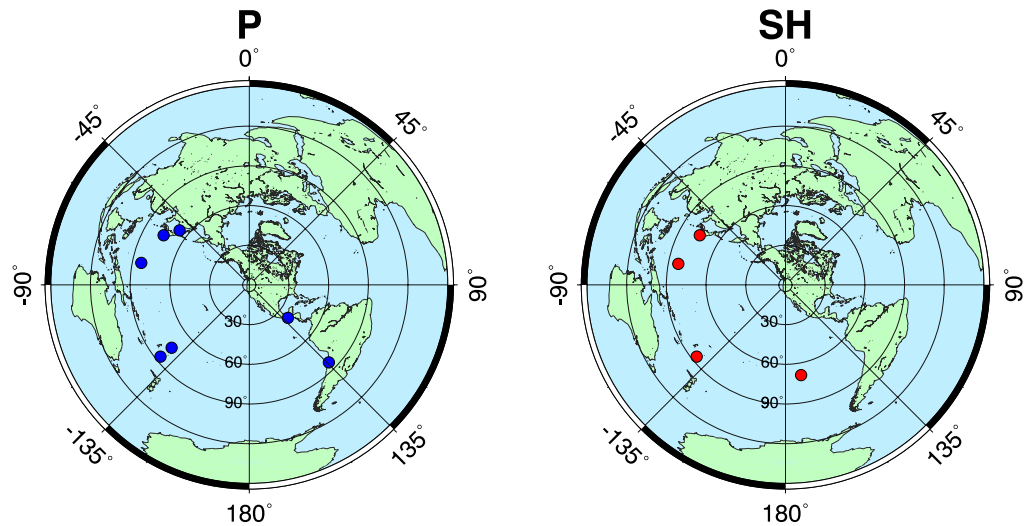


Figure 3. Teleseismic events for (a) P waves (b) and SH used in this study. Detailed event informations are given in Table 1.

of the spectral-element mesh. The mesh goes from the surface down to 300 km depth, the depth extension of the subducting slab in regional tomographic models beneath central Oregon (e.g., James et al., 2011; Obrebski et al., 2010). We use degree-7 Lagrange polynomials in the three orthogonal directions so that the geometry of each element is defined by $8 \times 8 \times 8 = 512$ nodes. The grid is composed of 35,112 spectral elements and 12,622,584 nodes or grid points. The minimum resolved period of this mesh is about 2 s. Our goal is to invert the values of density, V_p , and V_s at each node of the spectral-element mesh which will also be our tomographic grid.

2.4. Definition of the Cost Function

We invert the vertical and radial components of P waveforms, and the transverse component of SH waveforms. The time windows used in the inversions start 5 s before the main phase arrival and end 30–60 s after the phase (P or SH), depending on the event. These time windows are sufficiently long to include not only the direct phases but also all the reverberations and conversions on the main lithospheric interfaces.

The waveform inversion problem consists in finding the model \mathbf{m} that minimizes the cost function (Tarantola, 2005)

$$\chi(\mathbf{m}) = \frac{1}{2}(\mathbf{g}(\mathbf{m}) - \mathbf{u}_{\text{obs}})^t \mathbf{C}_D^{-1}(\mathbf{g}(\mathbf{m}) - \mathbf{u}_{\text{obs}}) + \frac{\lambda}{2}(\mathbf{m} - \mathbf{m}_{\text{prior}})^t \mathbf{C}_M^{-1}(\mathbf{m} - \mathbf{m}_{\text{prior}}), \quad (2)$$

where \mathbf{g} is the forward wave equation operator, \mathbf{C}_D the data covariance matrix, and \mathbf{C}_M the a priori model covariance matrix. The first term in Equation 2 quantifies the waveform misfits, where integration over selected time windows and summation over events and seismic phases is implicit. The second term quantifies the model deviation from the a priori model. The regularization parameter λ is introduced so that these two terms have balanced contributions to the misfit function.

2.5. The Full Waveform Inversion Method

The full waveform inversion method follows the general workflow described in Monteiller et al. (2015) and Kan et al. (2023), to which the reader is referred for further details. The forward wave-equation problem is solved with a hybrid numerical method (Monteiller et al., 2013, 2021) that couples AxiSEM (Nissen-Meyer et al., 2014) with a spectral-element method (SEM) in a regional domain (Komatitsch & Tromp, 1999). The principle is to compute and inject the incident wavefield on the edges of the SEM grid in order to limit the time-consuming 3D computations inside a small regional domain, thereby reducing the computational costs by several orders of magnitude.

Whereas it is common practice to consider a diagonal model covariance matrix, that is, to assume that model parameters are uncorrelated, Kan et al. (2023) have demonstrated that such assumption leads to inconsistent and

biased model reconstructions, and that accounting for the well-documented correlations between density and V_p , and between V_p and V_s , improved substantially the reconstructed density and velocity models. Following their approach, we consider a model covariance matrix of the form

$$\mathbf{C}_M = \begin{bmatrix} \sigma_\rho^2 \mathbf{C} & r\sigma_\rho\sigma_{V_p} \mathbf{C} & r\sigma_\rho\sigma_{V_s} \mathbf{C} \\ r\sigma_\rho\sigma_{V_p} \mathbf{C} & \sigma_{V_p}^2 \mathbf{C} & r\sigma_{V_p}\sigma_{V_s} \mathbf{C} \\ r\sigma_\rho\sigma_{V_s} \mathbf{C} & r\sigma_{V_p}\sigma_{V_s} \mathbf{C} & \sigma_{V_s}^2 \mathbf{C} \end{bmatrix}, \quad (3)$$

where r is the correlation coefficient between each pair of parameters, \mathbf{C} the spatial covariance kernel, σ_ρ the standard deviation of density, σ_{V_p} the standard deviation of V_p , and σ_{V_s} the standard deviation of V_s . For the spatial covariance of a given parameter between two points of the model located at \mathbf{r} and \mathbf{r}' , we consider an exponential kernel of the form

$$C(\mathbf{r}, \mathbf{r}') = e^{-\sqrt{\frac{|\mathbf{r}-\mathbf{r}'|^2}{\ell}}}, \quad (4)$$

where ℓ is the correlation (or smoothing) length. Its main advantage is that it admits the simple inverse operator

$$C^{-1}(\mathbf{r}, \mathbf{r}') = \frac{1}{8\pi\ell^3} (\mathbf{I} - \ell^2 \Delta)^2, \quad (5)$$

where Δ is the Laplacian operator (Oliver, 1998; Trinh et al., 2017). The values of the hyperparameters used in the inversions are given in Table 2.

2.6. The Iterative Inversion Algorithm

We search for the minimum of (2) with an iterative algorithm (e.g., Tarantola, 2005), in which the model \mathbf{m}_k at iteration k is perturbed by the quantity

$$\Delta \mathbf{m}_k = -\alpha_k \mathbf{H}_k^{-1} \cdot \gamma_k \quad (6)$$

where α is the step length, \mathbf{H}^{-1} the inverse Hessian, and γ_k the gradient of cost Equation 2 at iteration k . This gradient is given by

$$\gamma_k = \frac{\partial \chi_k}{\partial \mathbf{m}} = \mathbf{G}_k' \mathbf{C}_D^{-1} (\mathbf{g}(\mathbf{m}_k) - \mathbf{u}_{\text{obs}}) + \lambda \mathbf{C}_M^{-1} (\mathbf{m}_k - \mathbf{m}_{\text{prior}}), \quad (7)$$

with \mathbf{G}_k the derivative or Jacobian operator given by

$$\mathbf{G}_k = \frac{\partial \mathbf{g}}{\partial \mathbf{m}} (\mathbf{m}_k). \quad (8)$$

The first contribution to the gradient is computed with the adjoint method (Tromp et al., 2005). Instead of computing the inverse Hessian, we use its finite-difference approximation given by the L-BFGS method (Nocedal & Wright, 2006) from the model and gradients obtained at the previous iterations. We refer the reader to Monteiller et al. (2015) for a more detailed description of the L-BFGS method and its application to waveform inversion.

The hierarchical inversion starts at long period with data bandpass filtered between 25 and 10 s. We then run new inversions on data filtered with a lower corner period that is progressively decreased from 10 to 8, 6, and finally 4 s, using as a starting model the model obtained at the previous longer period inversion.

2.7. Event Normalization

Our teleseismic data set contains events with different magnitudes, ranging between 6.2 and 7.5 (Table 1). We thus need to normalize the gradients of each event so that all the events contribute equally to model reconstruction. Since each event gradient is obtained by correlating the direct and adjoint wavefields (Tromp et al., 2005), we define a normalization that scales with the product of the characteristic amplitudes of the direct and adjoint wavefields. Because the adjoint wavefield is the solution of the wave equation with the adjoint sources that are

the time-reversed waveform residuals at each station, it scales with the root mean square waveform residual. The normalization N_k for event k is thus defined by

$$N_k = \frac{1}{N(t_2 - t_1)} \sqrt{\sum_{i=1}^N \int_{t_1}^{t_2} s_i^2(t) dt} \cdot \sqrt{\sum_{i=1}^N \int_{t_1}^{t_2} [s_i(t) - u_{obs,i}(t)]^2 dt}, \quad (9)$$

where $s_i(t)$ and $u_{obs,i}(t)$ are respectively the synthetic and observed seismograms at station i . For P waveforms, we use the vertical component to compute the normalization factors whereas for SH waveforms we use the transverse component. These normalization factors are computed at the beginning of each inversion and remain the same during iterations.

3. Results

Figure 6 shows the evolution of the normalized cost function during the inversions in the different frequency bands. The misfit reduction is about 80% in the long-period inversion. Note that the misfit reductions are not directly comparable because they are normalized by the misfit of the starting model, which is not the same in the different inversions.

3.1. Tomographic Model Obtained After Hierarchical Inversion

The final density, V_p , and V_s models obtained after hierarchical inversion are shown in Figure 7, using both absolute and relative scales. The most salient feature is the eastward dipping low-velocity zone (LVZ) on the western side of the profile, with compressional velocities between 5.6 and 6.2 km/s and shear velocities between 3.2 and 3.5 km/s. The top of this LVZ, observed between 20 and 40 km depth, coincides with the contour of the subducted JdF slab (Hayes et al., 2018). Since the minimum period in the inversions is 4 s, its thickness is not well resolved, but we can estimate it to be less than 10 km.

The LVZ is also characterized by a rather large V_p/V_s ratio ~ 1.9 . Even though this feature is on the margin of what is confidently resolved by our inversion, such a large V_p/V_s ratio is in rather good agreement with estimation coming from the modeling of receiver function which suggests even larger values, that can reach up to 2.2 (Audet et al., 2009; S. M. Peacock et al., 2011). The LVZ has a shallower dipping angle in its eastern termination, which is consistent with the results obtained in the inversion of short-period scattered body waves (Rondenay et al., 2001; M. G. Bostock et al., 2002). We note that the horizontal extension of the LVZ is strongly correlated with the epicentral location of tremors given by Wech (2021) (Figure 14). From 40 to 60 km depth, seismic velocities as well as density progressively increase downdip and reach values of about 8 km/s for V_p , 3.5 km/s for V_s , and $3.5 \text{ g} \cdot \text{cm}^{-3}$ for density. A similar though less pronounced velocity increase is observed in the subducting oceanic mantle, which has a clear signature beneath 50 km depth. The upper limit of this high-velocity body again closely follows the contour of the JdF slab.

To the east of the section, that is, beneath the High Cascades and Deschutes Basin, sharp contrasts in density and V_p , and to a lesser extent in V_s , are observed across a nearly flat Moho, located at about 35 km depth. This is in excellent agreement with the results of the inversion of short-period scattered teleseismic body waves (Rondenay et al., 2001; M. G. Bostock et al., 2002). In contrast, beneath the Willamette Valley and the western part of the western Cascades, a smooth, weak gradient in density and seismic velocities is observed at the crust-mantle boundary. This reduced impedance contrast explains the disappearance of the Moho in the migrated sections beneath the forearc (Rondenay et al., 2001; M. G. Bostock et al., 2002; Tauzin et al., 2016) and in the wide-angle reflection sections (Trehu et al., 1994). It results from a combination of high density and seismic velocities in the forearc crust and low density and seismic velocities in the forearc mantle wedge. Active source seismic experiments have documented high V_p in the forearc, reaching 6.5 km/s at 11 km depth (Trehu et al., 1994), in rather good agreement with our V_p model. These high velocities have been attributed to a block of oceanic crust, the Siletz terrane, accreted to North America ~ 50 Ma ago. The results of these active source experiments also demonstrated southward crustal thickening in the Siletz terrane, from 6 km north to at least 20 km south in central Oregon (Trehu et al., 1994). Such a large crustal thickness could be related to an oceanic plateau formed above a hotspot near the Farallon-Kula plate boundary (Trehu et al., 1994; Wells et al., 2014). The forearc mantle wedge is characterized by a density around $3.0 \text{ g} \cdot \text{cm}^{-3}$, V_p around 7.0 km/s, and V_s around 3.8 km/s, which represents a reduction of about 15% compared to the values of a typical continental lithospheric mantle. This suggests a high degree of serpentinization which can be estimated at about

30%, considering the experimental data from Christensen (1966) and Christensen (2004). This value is about half of the indirect estimate obtained from the analysis of scattered teleseismic waves, which is of the order of 50%–60% (M. G. Bostock et al., 2002). At shallow depth (<10 km), we image three low-velocity regions in the accretionary prism, the Willamette Valley and the Deschutes Basin, which have a particularly clear signature in the V_p/V_s model.

The V_p/V_s ratio model displays several interesting features. The western Cascades crust is characterized by a V_p/V_s ratio lower than 1.65. Such low values, which are well below those of typical crustal rocks (e.g., Brocher, 2005; Christensen, 1996), have been previously documented in local earthquake tomography studies of the Cascadia forearc crust (Guo et al., 2021; Ramachandran & Hyndman, 2012; Savard et al., 2018). In contrast, beneath the Willamette Valley and part of the Coastal Range, that is, in the Siletz terrane (Wells et al., 2014), the V_p/V_s ratio is comprised between 1.7 and 1.8, which suggests a more mafic composition. Near the surface and below the coastal range, V_p/V_s is larger than 1.9, as expected for sediments saturated in fluids in the accretionary wedge. The sediments in the Willamette Valley have also a clear signature in the V_p/V_s model, in good agreement with the local earthquake tomography performed by Dunham and Kiser (2020). Beneath the volcanic arc, a shallow prominent positive V_p/V_s anomaly is imaged, that could be related to a magma reservoir. Finally, a prominent high V_p/V_s anomaly larger than 1.9 is observed, around 75 km beneath the volcanic arc. This region is also characterized by reduced density and seismic velocities, which could suggest the presence of melt.

3.2. Waveform Fits

The P and S waveform fits for event 9 are shown in Figure 8. We compare the observed (black lines) and synthetic (red lines) seismograms computed in the initial smooth 1-D model and in the final 3-D model (Figure 7). For P waves, the fit of the vertical component before inversion is much better than the radial component. This results from the fact that the vertical component of teleseismic P waves is dominated by the direct P wave, which is highly coherent at the regional scale. It is this very property that allows us to make robust estimate of the average incoming P wavelet. The P reverberations, such as the PmP phase reflected on the Moho, generally have small amplitudes, of the order of a few percent compared to the directly transmitted P wave. The vertical component misfits thus mainly reflect the small amplitude and travel time residuals of the P wave at each station. The radial component, on the other hand, is characterized by a more evenly distributed energy in the selected time window. Secondary arrivals in the P wave coda, such as P-to-S conversions and reflections on seismic discontinuities, have amplitudes comparable to the direct P wave on the radial component. On the western part of the transect, the signature of eastward dipping interfaces, most likely related to the LVZ, is clearly observed. Because the initial model is a smooth 1-D model, the radial component synthetic seismograms computed in this model provide a poor fit of observed data. The transverse component of SH waves is also dominated by the direct SH wave, with strong later-arriving reverberations. Note that the time window selected for the inversion of SH waveforms is shorter than the one for P waveforms, in order to exclude the ScS and SKS waves that arrive ~40 s after the S wave. After inversion, the improvement of P and SH waveforms fits is spectacular (>80%), not only for the energetic P and SH waves but also for the later arriving scattered waves.

3.3. Synthetic Resolution Test

To estimate the resolution potential of our FWI, we performed a synthetic inversion experiment on the subduction model from Kan et al. (2023). In this study, they considered a regular 2D array of receivers with a 10 km spacing and four teleseismic sources in backazimuth of 0°, 70°, 180°, and 300°. This new synthetic inversion experiment allows studying the limitation resulting from the 1D CASC93 acquisition. The models obtained after hierarchical inversion of the synthetic seismograms computed for the P and SH teleseismic sources are shown in Figure 9 down to 4 s period. The main features of the subduction model such as the sedimentary basin, the subducting plate, and the serpentinized mantle wedge are correctly reconstructed. However, the V_p/V_s model is contaminated by significant artifacts even though the main features of the input model are distinguishable. This simple inversion experiment thus suggests that the CASC93 experiment data set should indeed provide robust models of density, V_p , and V_s down to 150 km depth.

4. Discussion

4.1. The Impact of Adding SH Waveforms and Accounting for the Correlation Between Model Parameters

To investigate the impact of adding SH waveforms and of the a priori assumption that model parameters are correlated, we performed three additional hierarchical inversions:

- Inversion of only P waveforms with a diagonal model covariance matrix, that is, assuming that model parameters are uncorrelated
- Inversion of both P and SH waveforms with a diagonal model covariance matrix
- Inversion of only P waveforms with a complete model covariance matrix

The waveform fits for event 9 obtained after these three hierarchical inversions and the ones already presented in the previous section are shown in Figure 10. The reduction of the vertical and radial P waveform misfits for this event is similar in the four inversions. The main difference is observed for the SH waveform fits, which are greatly improved when SH waveforms are included in the inversions. Inverting only the P waveforms with a complete covariance matrix yields intermediate fits for the SH waveforms (40% misfit reduction), suggesting that accounting for the correlation between V_s and density and between V_s and V_p partially compensates for the absence of SH waveforms for the V_s model reconstruction.

Figure 11 gives the waveform misfits computed on the complete data set. We again observe similar P waveform fits in the four inversions, with a slighter larger misfit reduction on the vertical component compared to the radial component. A good SH waveform fit is only obtained when SH waves are included in the inversion.

Whereas the four inversions provide quasi-identical P waveform fits, the final V_p models differ substantially (Figure 12). The models obtained with a diagonal model covariance matrix, that is, assuming that density and seismic velocities are not correlated, only show long wavelength structures such as the crust and its lateral thickness variations, as well as the subducting slab. Structural details such as the LVZ, which has a strong signature on the radial component of P waves (Figure 7c), is not retrieved at all. On the other hand, it is seen in the density models, as well as in the V_s models, but with a reduced amplitude of the low-velocity anomaly. Intuitively, this can be understood by the fact that for a given frequency content, the wavelength of P waves is about twice that of S waves, and since in FWI the resolution approximately scales with the wavelength (e.g., Virieux & Operto, 2009) a sharper resolution is indeed expected in the V_s model. Another reason is that the V_p model is mainly reconstructed from transmitted P waves, whereas for the density and V_s models the dominant contribution comes from P-to-S conversions and reflections. The former are mainly sensitive to long wavelength structures whereas the latter are mainly sensitive to sharp gradients and discontinuities. A consequence of the uneven resolution in the V_p and V_s models is that the V_p/V_s model is poorly constrained, and with strong artifacts, notably in the forearc, where extreme values lower than 1.50 are observed (Figures 12d and 12h).

These results underscore the non-unique solutions of FWI and the intrinsic trade-offs between density, V_p , and V_s . Small waveform misfits therefore cannot be interpreted as a reliable indicator of the quality of the inversion results. Other informed criteria describing our degree of knowledge on model parameters need to be considered. Our results confirm that accounting for the well-documented correlations between V_p and V_s , and between density and V_p (or V_s) lead to better-resolved models, especially of V_p and V_s models at depth. The common assumption (often made implicitly) that model parameters are not correlated, has a strong detrimental effect on the results of FWI.

The addition of SH waveforms, which were not considered in previous applications of FWI on real data (Y. Wang et al., 2016; Beller, Monteiller, Operto, et al., 2018; K. Wang et al., 2021; Chevrot et al., 2022), has also a beneficial though less noticeable effect. Whereas large-scale structures in the V_s models shown in Figures 12k and 12o are extremely similar, small-scale structures such as the LVZ, the serpentinized mantle wedge, or the low-velocity anomaly around 75 km depth beneath the volcanic arc, are more sharply defined in the inversion that includes SH waveforms.

An important limitation of FWI of teleseismic P waves comes from reverberations in sedimentary basins. In the earlier applications of FWI in the Pyrenees region, strong artifacts were indeed observed in the crust and shallow mantle beneath the Aquitaine Basin (Y. Wang et al., 2016; K. Wang et al., 2021; Chevrot et al., 2022). Similar artifacts are observed in the eastern part of the section, beneath the Deschutes Basin, where values of V_s larger than 4.0 are observed in the lower crust (Figure 12k). Delph et al. (2018) also reported very

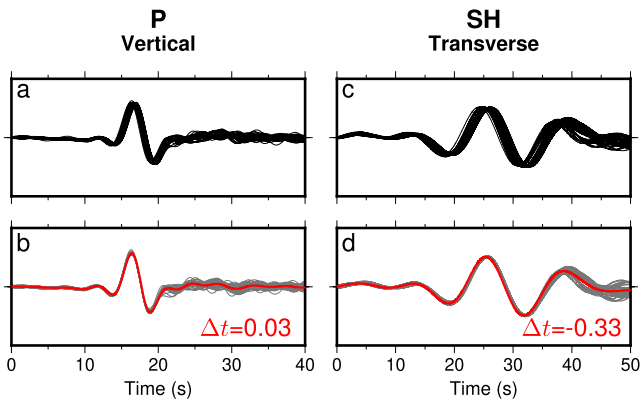


Figure 4. Illustration of the source wavelet estimation procedure on event 9 (see Table 1). The vertical and transverse components are used for P and SH waveforms, respectively. (a) Observed vertical components filtered in the period band 10–25 s. (b) Time-aligned traces (gray lines) after being deconvolved from the corresponding Green's functions and the average source wavelet (red line). (c, d) Same as (a, b) but for the transverse component SH waveforms. The average time shift Δt is used to correct the timing of the source wavelet so that for each event the average travel time residual is zero.

high shear velocities in the crust from their joint inversion of surface wave dispersion curves and receiver functions. In contrast, values more typical of a continental lower crust (between 3.6 and 3.8 km/s) are obtained after joint inversion of P and SH waveforms (Figure 12o). Therefore, transmitted shear waves seem to provide sufficient independent information to correct the velocity model from the detrimental effects of reverberations on shallow interfaces such as the basement of sedimentary basins, which leads us to advocate the exploitation of shear waves in future applications of FWI. Beller and Chevrot (2020) came to a similar conclusion regarding the importance of jointly inverting compressional and shear waveforms for proper 3-D imaging of seismic anisotropy. We can thus foresee a growing interest in performing such joint P and S inversions in the near future.

4.2. Comparison Between FWI, Travel Time Tomography, and Scattered Waves Inversion

Figure 13 shows the comparison between our V_S model and some published V_S models obtained by regional travel time tomography in a vertical cross-section that follows the CASC93 transect line. The geometry of the long-wavelength fast velocity anomaly which corresponds to the JdF subducting plate is fairly consistent in all these models. However, the FWI model appears to contain a wealth of details at shallow depth (<100–150 km that are completely absent in the models derived from travel time tomography). This marked difference in resolution between FWI and travel time tomography stems from the fact that the latter only exploits the phase of the direct P or S phases. Therefore, only long-wavelength structures are correctly resolved. Moreover, since teleseismic body waves have subvertical angles of incidence, tomographic images suffer from poor sensitivity in the shallow part of the model where there is little ray crossing as well as strong vertical smearing. In contrast, FWI exploits the complete seismic wavefield and the contribution of scattered phases strongly increases the sensitivity to small-scale heterogeneities and to density. However, owing to geometrical spreading, the sensitivity of scattered waves to structural discontinuities decreases as depth increases. It is also limited by the finite duration of the temporal windows that are inverted, which can potentially suppress the contribution of waves scattered on very deep discontinuities. In the long-period FWI, the dominant period of seismic waves is longer than 10 s. This means that the wavelength of P waves is greater than 80 km and the wavelength of S waves is greater than 50 km. Therefore, the asymptotic description of the wavefield in terms of well-isolated direct or scattered P and S waves is no longer valid up to ~ 100 km depth (Favier et al., 2004). In this depth interval, the near-field and mid-field terms are not negligible. The transition to the asymptotic far-field regime at depth also corresponds to a sharp decrease in the amplitude of the gradient (see Figure 6 in Monteiller et al. (2015)). This sharp decrease in sensitivity where the distance

Table 1
List of Teleseismic Events Selected for Waveform Inversion

Event	Phases	Origin time	Location (lat, lon)	Depth (km)	Dist. (°)	Baz (°)	M_w
1	P	1993/05/16 21:44:50.0	15.34 S, 173.35 W	33	75.4	231	6.6
2	SH	1993/07/06 02:53:03.9	24.56 S, 111.86 W	10	69.3	170	6.3
3	P	1993/07/11 13:36:19.2	25.35S, 70.18 W	33	84.2	134	6.6
4	P	1993/07/12 13:17:11.9	42.84 N, 139.25 E	17	66.7	308	7.3
5	P + SH	1993/08/07 17:53:27.0	23.87 S, 179.82 E	555	86.1	231	6.7
6	P	1993/08/08 08:34:25.0	12.96 N, 144.78 E	61	83.1	282	7.5
7	SH	1993/08/11 14:17:41.7	13.13 N, 145.62 E	56	82.3	281	6.2
8	P	1993/09/10 19:12:54.8	14.73 S, 92.68 W	34	38.9	130	7.2
9	P + SH	1993/10/11 15:54:22.4	32.00 N, 137.85 E	365	74.6	300	6.8

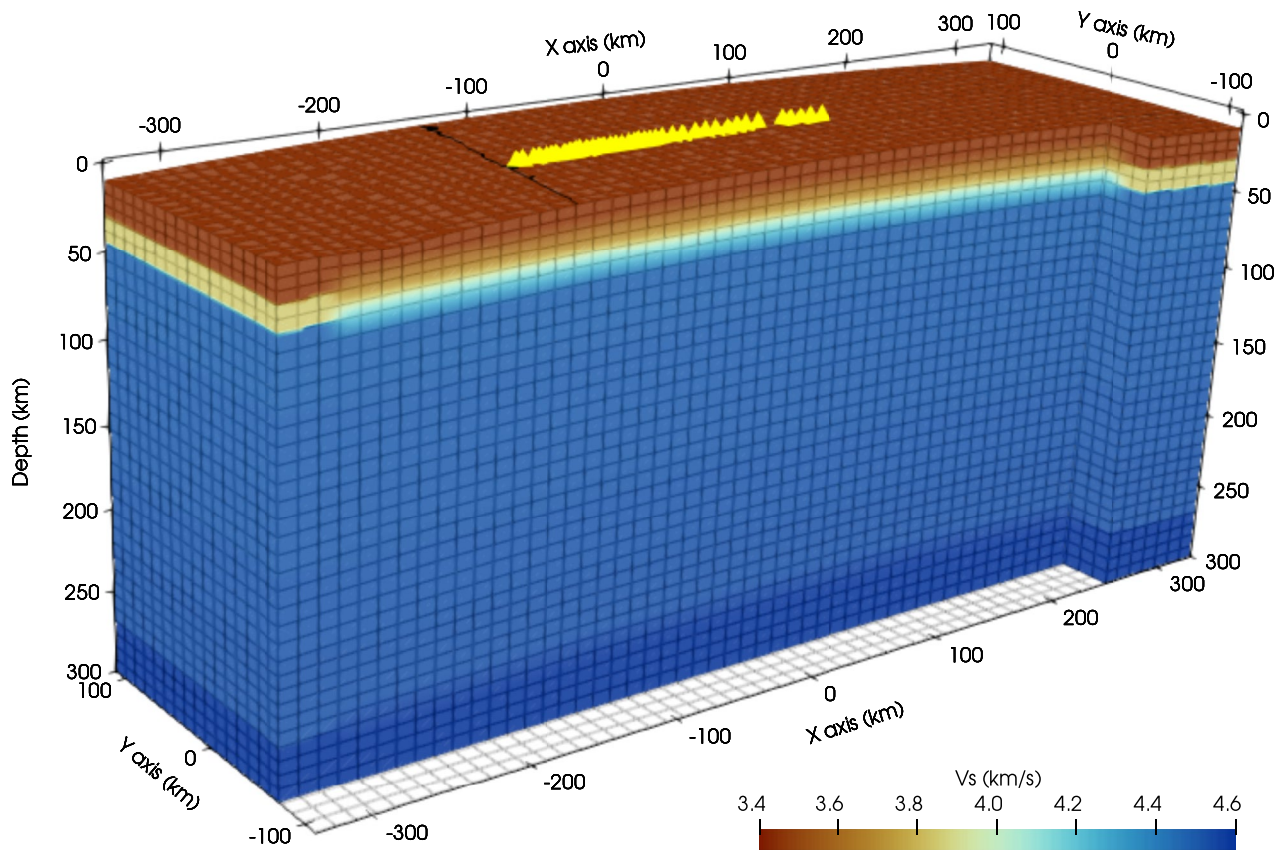


Figure 5. Spectral-element mesh. The number of elements along the x, y, and z directions are 56, 19, and 33, respectively. The yellow triangles show the positions of the stations from the CASC93 experiment that were used in this study. The black contour shows the coastline. The background colors in the grid show the initial V_S model, a smoothed version of the ak135 reference Earth model. Note the velocity model near the boundary of the mesh is specified for the layered ak135 model, to be consistent with the one used to compute the external wavefield.

from seismic stations exceeds about one wavelength results from the fact that in the far-field regime, the main contribution comes from directly transmitted waves, with much weaker contributions from scattered waves. Because the number of teleseismic events with a sufficiently high S/N ratio is generally small, especially when dealing with short-duration deployments such as the CASC93 Experiment, the ray coverage at depth is quite poor, in contrast to travel time tomographic studies that often rely on $\sim 10^5$ – 10^6 travel time picks. For example, in their tomography of the mantle beneath the United States (Schmandt & Lin, 2014), used 516,688 P and PKP traveltimes, and 223,462 S and SKS travel times.

In Figure 14, we superpose our V_S model on the results obtained by the inversion of short-period teleseismic P waves coda, which exploits the different scattering modes to reconstruct the geometry of seismic discontinuities in the underlying medium (Rondenay et al., 2001; M. G. Bostock et al., 2002). A remarkable agreement is observed with our velocity model, in particular for the geometry of the LVZ and of the Moho in the upper plate. The absence of a clear Moho signature was attributed to the presence of higher seismic velocities in the lower

forearc crust and lower velocities in the serpentinized mantle wedge (M. G. Bostock et al., 2002). This interpretation is in excellent agreement with our 3D V_S model. Migration of scattered waves also documented a weaker signature of the oceanic crust below ~ 50 km depth (Rondenay et al., 2001; M. G. Bostock et al., 2002; Tauzin et al., 2016), which is also in good agreement with our FWI results. These studies also detected a dipping interface characterized by a downward velocity reduction between 50 and 100 km depth beneath the oceanic Moho. This interface has been attributed to the upper

Table 2
Hyperparameters Used in the Inversions

Periods	σ_{V_p} (km/s)	σ_{V_s} (km/s)	σ_ρ (g/cm ³)	r	ℓ (km)
25–10, 8, 6 s	0.65	0.37	0.27	0.97	5
25–4 s	0.65	0.37	0.27	0.80	5

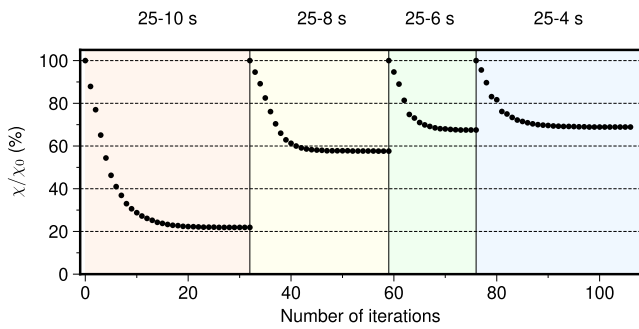


Figure 6. Evolution of cost function reductions for the four hierarchical inversions with progressively reduced lower corner period of 10, 8, 6, and 4 s. The misfits are normalized to 100% when we start the new inversion in a shorter period.

boundary of a layer of frozen anisotropy resulting from the alignment of olivine crystals near the ridge (Tauzin et al., 2016). We find no evidence for a such velocity reduction in our model.

4.3. The Geometry of the Subducting Juan de Fuca Plate

The Slab2 subduction zone model (Hayes et al., 2018) is built from a compilation of seismicity catalog and tomographic models. In Cascadia, due to the paucity of the earthquake catalog, the JdF plate is primarily constrained by published travel time tomography models such as those shown in Figure 13. Although these different models differ in detail, they show consistent long-wavelength structures with a fast anomaly down to about 200 km depth approximately following the slab contour from the Slab2 model. They also show a pronounced low-velocity anomaly beneath the backarc between 100 and 300 km depth. Our FWI model is in good agreement with these first-order features.

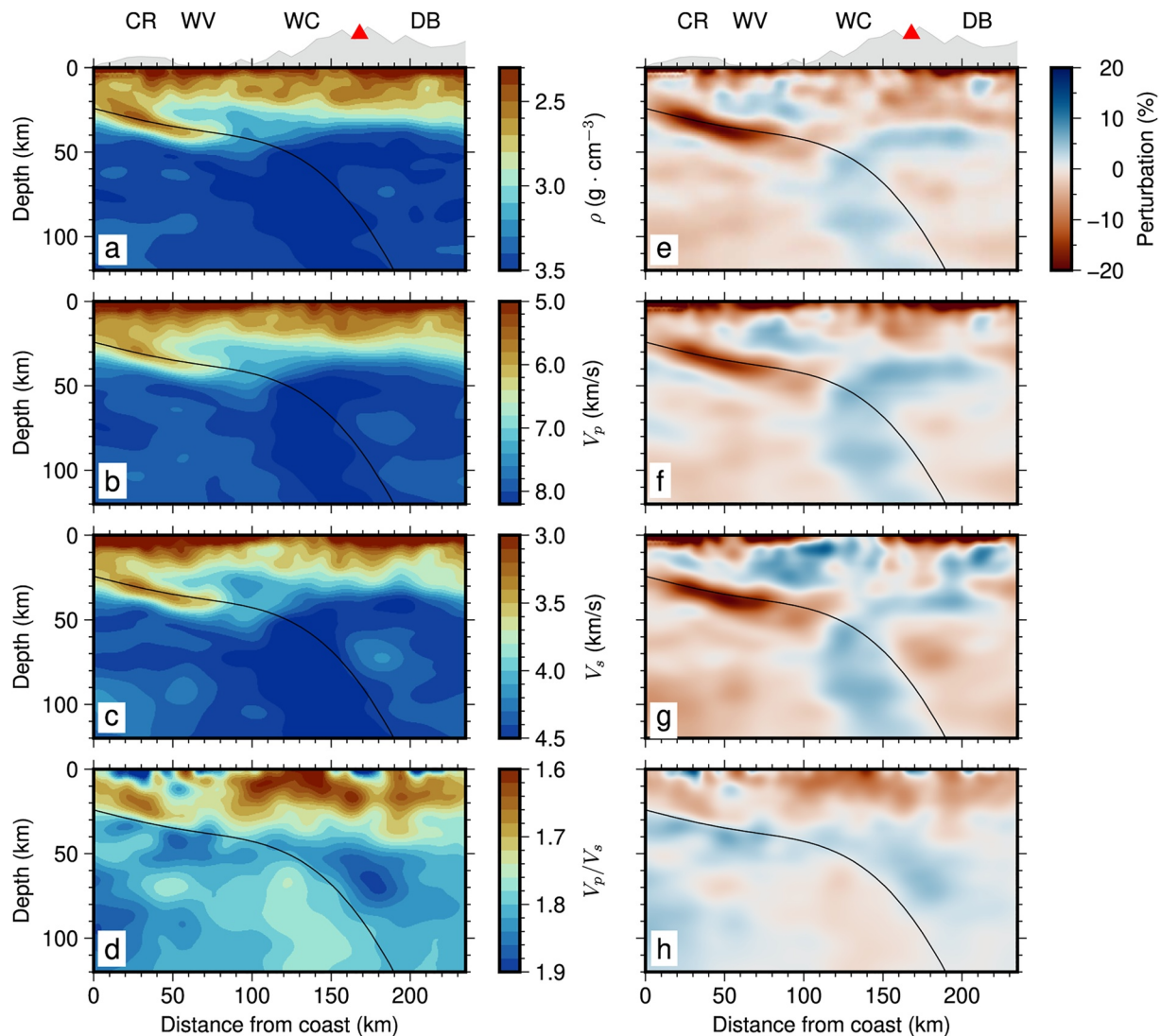


Figure 7. Results of the hierarchical full waveform inversion. Left: models of absolute (a) density, (b) V_p , (c) V_s , and (d) V_p/V_s . Right: perturbations of (e) density, (f) V_p , (g) V_s , and (h) V_p/V_s with respect to the initial 1-D smooth ak135 model. The black line shows the slab contour of the JdF plate taken from Hayes et al. (2018), and the red triangle marks the position of Mount Jefferey in the volcanic arc. Physiographic provinces are the same as specified in Figure 1.

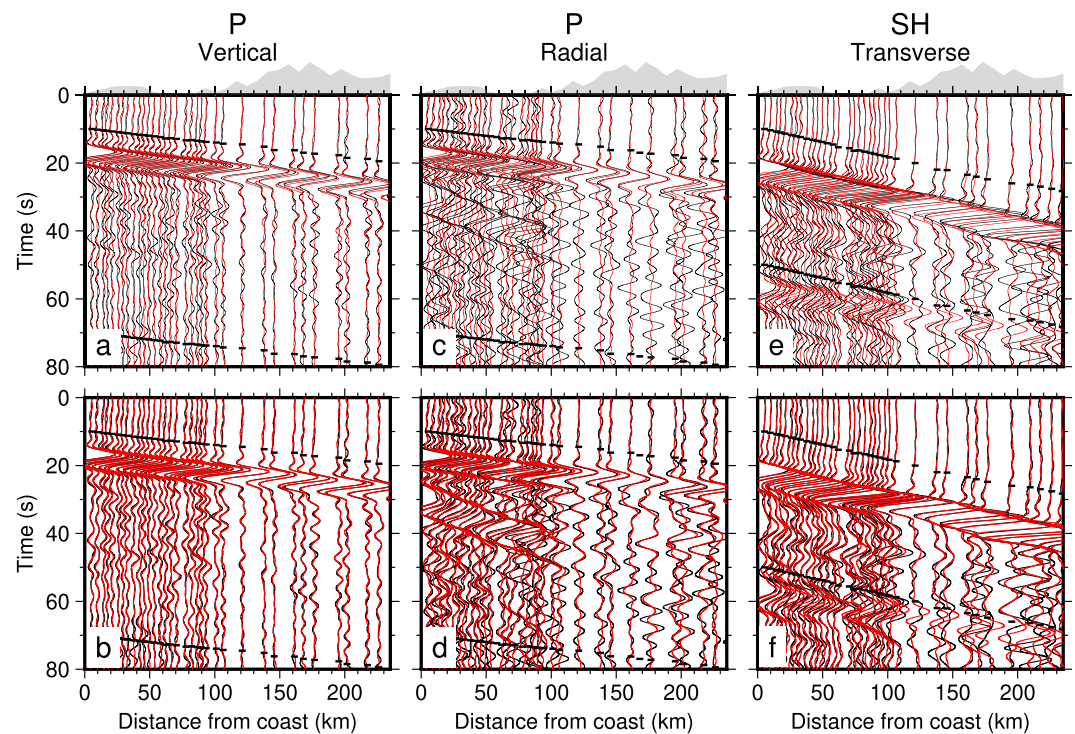


Figure 8. Waveform fits for event 9 at filtered between 4 and 25 s period (see Table 1). Observed (black lines) and synthetic (red lines) vertical component P waveforms computed in the initial (a) and final (b) models. Observed (black lines) and synthetic (red lines) radial component P waveforms computed in the initial (c) and final (d) models. Observed (black lines) and synthetic (red lines) transverse component SH waveforms computed in the initial (e) and final (f) models. The black ticks on each trace indicate the beginning and end of the time windows used in the inversion. The reductions of cost functions for the vertical, radial, and transverse components for this event are 85%, 81%, and 89%, respectively. The secondary arrivals observed ~ 40 s after the S wave in (e,f) are the SKS and ScS phases.

The increase of slab dip around 50 km depth corresponds to the completion of eclogitization reactions in the oceanic crust. These dehydration reactions are associated with an increase in the density of the oceanic crust that makes the plate negatively buoyant. Eclogitization of the oceanic crust could thus explain the apparent change in slab dip. In contrast, the results of scattered wave inversion (Rondenay et al., 2001; M. G. Bostock et al., 2002; Tauzin et al., 2016), based on the negative polarity interface imaged between 50 and 100 km, favor a smaller dip of about 20° , close to that of the LVZ. With such a geometry, the low seismic velocities observed around 100 km depth in our model (Figure 14) could be related to the partial melting of the subducting oceanic crust. Numerical modeling experiments suggest that partial melting of a subducting oceanic crust is indeed possible in subduction zones where very young oceanic lithosphere is being subducted, such as in the Cascade Range (S. M. Peacock et al., 1994). Although this hypothesis cannot be excluded, we tend to favor the first hypothesis which is more consistent with tomographic models of the Cascade Range. Regarding the disappearance of the fast anomaly below 200 km depth, since our model has a very limited spatial resolution in this depth range, our study does not shed new light on this long-standing controversy.

4.4. Fluid Migrations, Melting, and Metamorphic Reactions in the Central Cascadia Subduction Revealed by FWI

Our tomographic image (Figure 7) reveals the 3-D structures of the Cascadia subduction in central Oregon with a wealth of details that provide crucial insight into fluid migration and related metamorphic mineral reactions in the subduction factory. Our interpretations of the model are summarized in Figure 13.

The nature of the ubiquitous low-velocity layer beneath the Cascadia forearc, which is a prominent feature of our tomographic model, has been discussed by M. Bostock (2013). It is thought to be composed of hydrated

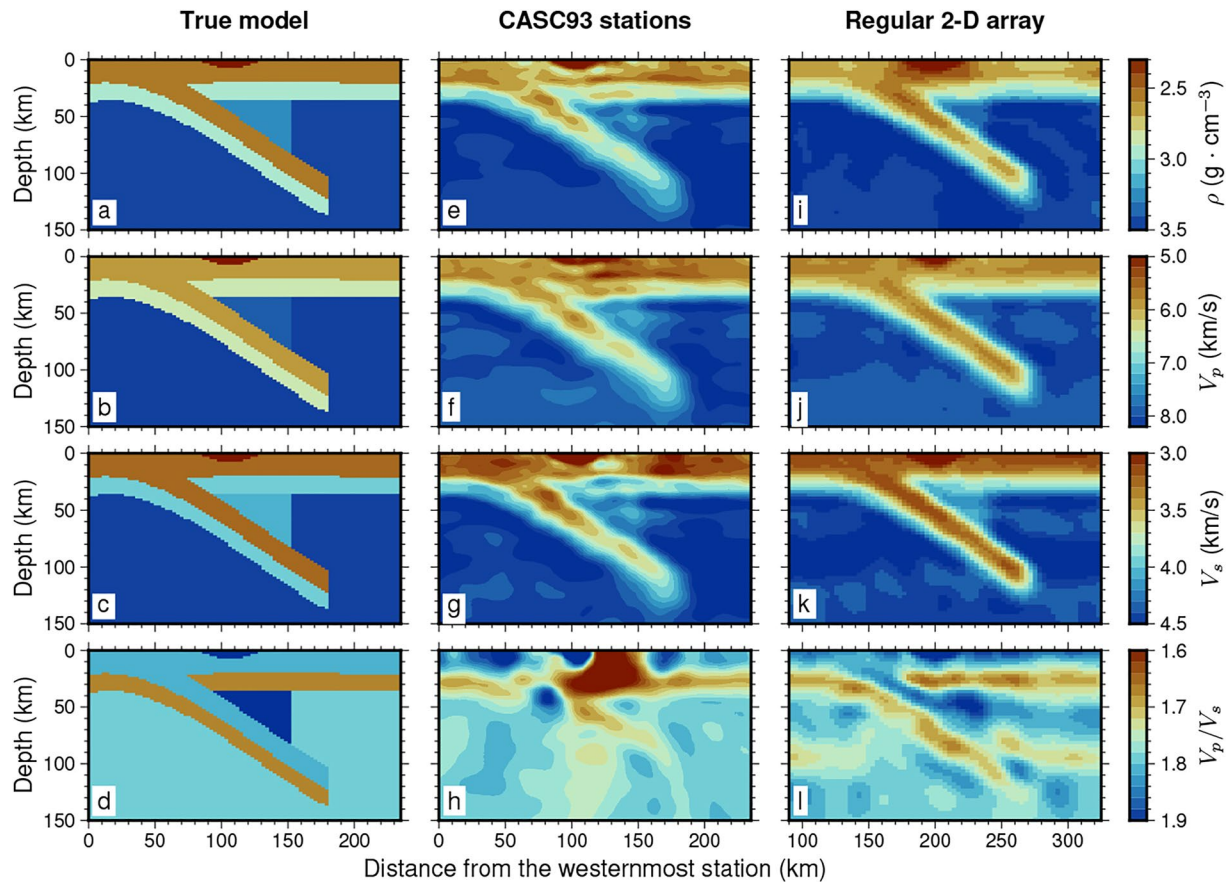


Figure 9. Reconstructions of the synthetic subduction model. (a–d) True model. (e–h) Inverted models using the CASC93 stations and the selected events in Table 1. (i–l) Inverted models using the source-receiver configuration considered in Kan et al. (2023), with a regular 2-D array and four teleseismic sources in backazimuth of 0°, 70°, 180°, and 300°. Each column shows models of absolute density, V_p , V_s , and V_p/V_s from the first row to the fourth row.

sediments and pillow basalts. Dehydration reactions release fluids that remain trapped between a low permeability seal above the subduction interface and an underlying layer of low-porosity gabbroic rocks. Tremors in central Cascadia are weaker and less frequent than in northern or southern Cascadia (Wech, 2021). Episodic tremor and slip (ETS) (Rogers & Dragert, 2003) locations from the Pacific Northwest Seismic Network (<https://pnsn.org/tremor>) (Wech, 2021) are closely related to the LVZ (Gosselin et al., 2020), which suggests a hydrologic control of slow slip events and tremors. The depth of tremors is not well constrained, especially in central Oregon where the station distribution is rather sparse. They probably occur at the subduction interface (black stars in Figure 15), as do the low-frequency events to which they are strongly related (Thomas & Bostock, 2015). However, a depth distribution of tremors over a depth range exceeding 40 km has been documented beneath southern Vancouver Island (Kao et al., 2005). Relocating tremors in finely resolved structural models such as the one obtained in this study could potentially improve our understanding of the fluid processes that produce these enigmatic events.

In our model, we observe a strong contrast between the backarc mantle and the forearc mantle, where density and seismic velocities are reduced by about 15% compared to the backarc mantle. The limit between these two domains is quite sharp and approximately follows the geometry of isotherm 600° in the thermal structure calculated for a hot continental subduction (Hyndman and Peacock (2003); Figure 4a). The transition from a low-permeability layer interface to a high-permeability layer interface corresponds to the onset of eclogitization of the oceanic crust (Audet et al., 2009). The eclogitization domain is clearly observed in our model, between the LVZ and the eclogitic crust, where the density and seismic velocities are close to those of the surrounding mantle. The width of this eclogitization domain, which is about 40 km, allows us to estimate the kinetics of the reaction. The velocity of the JdF subducting plate is about 4 cm/year (DeMets et al., 1990) and thus a complete eclogitization of the oceanic crust takes ~1 Myr. This is an important conclusion since eclogitization reactions

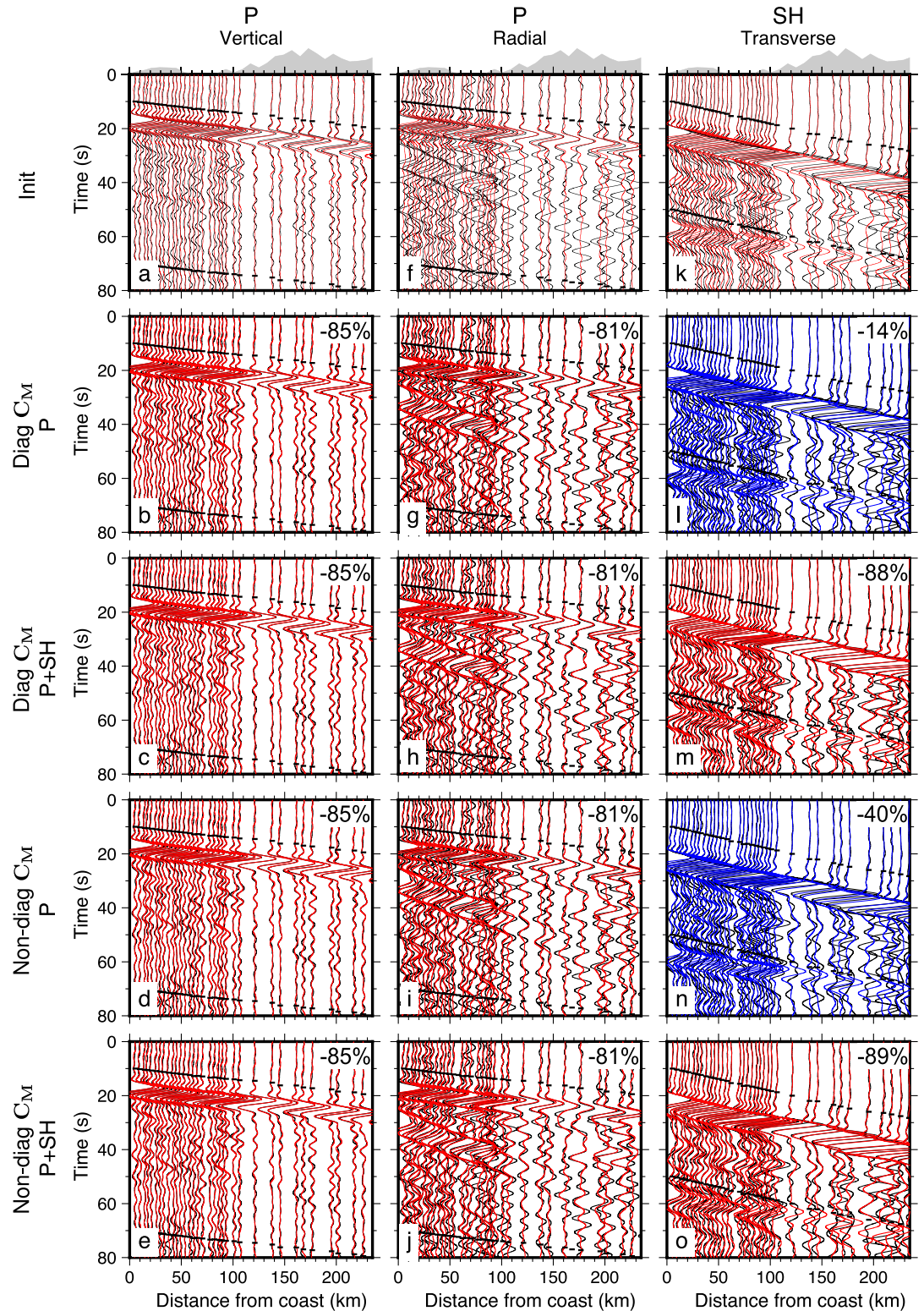


Figure 10. Waveform fits for event 9 obtained after the four hierarchical inversions. The solid lines show the observed seismograms and the red lines show the synthetic seismograms. The blue lines show the SH synthetic seismograms that were obtained in the two inversions in which only P waveforms were inverted. The cost reduction in percentage for each component after hierarchical inversion is specified at the upper-right of each panel.

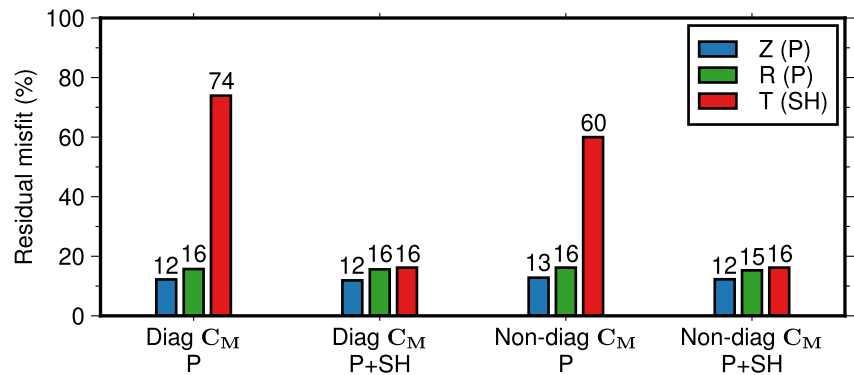


Figure 11. Residual misfits for the different types of inversions, defined as the ratio between the misfit in the final and the misfit in the initial smooth 1-D model (in percents).

control the buoyancy of subducting plates. Such a rapid reaction rate suggests that the subduction of an oceanic plateau is unlikely to support flat subduction, as suggested by geodynamic modeling studies (Gerya et al., 2009; van Hunen et al., 2002).

The transformation of hydrated metabasalts to eclogite releases a large amount of water into the overlying mantle wedge. This water will hydrate the olivine minerals in the peridotites, producing serpentine minerals (Hyndman & Peacock, 2003). Serpentine and hydrous minerals significantly alter the physical and mechanical properties of the forearc mantle, with density and seismic velocities reduced in proportion to the degree of serpentinization (Christensen, 2004). Back-arc mantle is too hot for hydrous minerals to be stable (Hyndman & Peacock, 2003). Serpentinization thus leads to a weak and buoyant forearc mantle wedge, isolated from the subduction-related circulation flow. The eastward limit of the serpentinized mantle wedge is quite sharp, and approximately corresponds

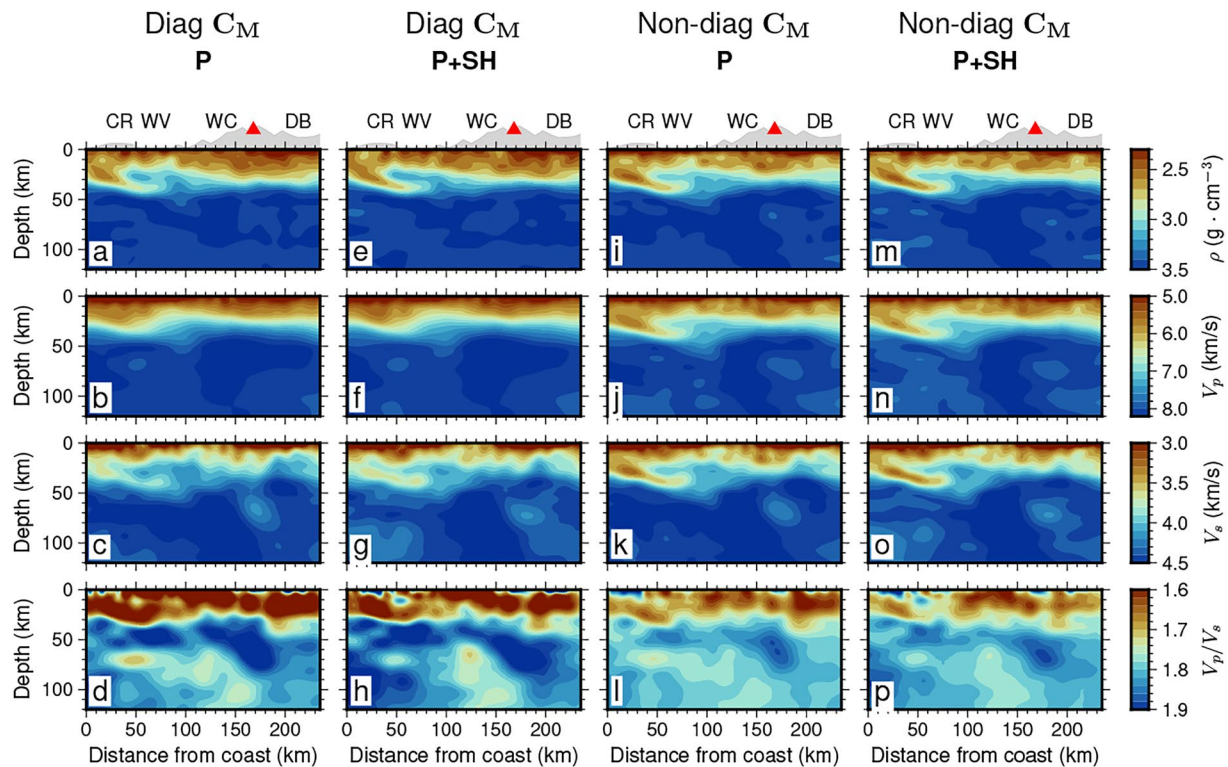


Figure 12. Results of the hierarchical FWI with different inversion strategies. Each column shows models of absolute density, V_p , V_s , and V_p/V_s from the first row to the fourth row. (a–d) Inversion with P events and a diagonal covariance matrix. (e–h) Inversion with P and SH events and a diagonal covariance matrix. (i–l) Inversion with P events and a non-diagonal covariance matrix. (m–p) Same as Figures 7a–7d. Inversion with P and SH events and a non-diagonal covariance matrix.

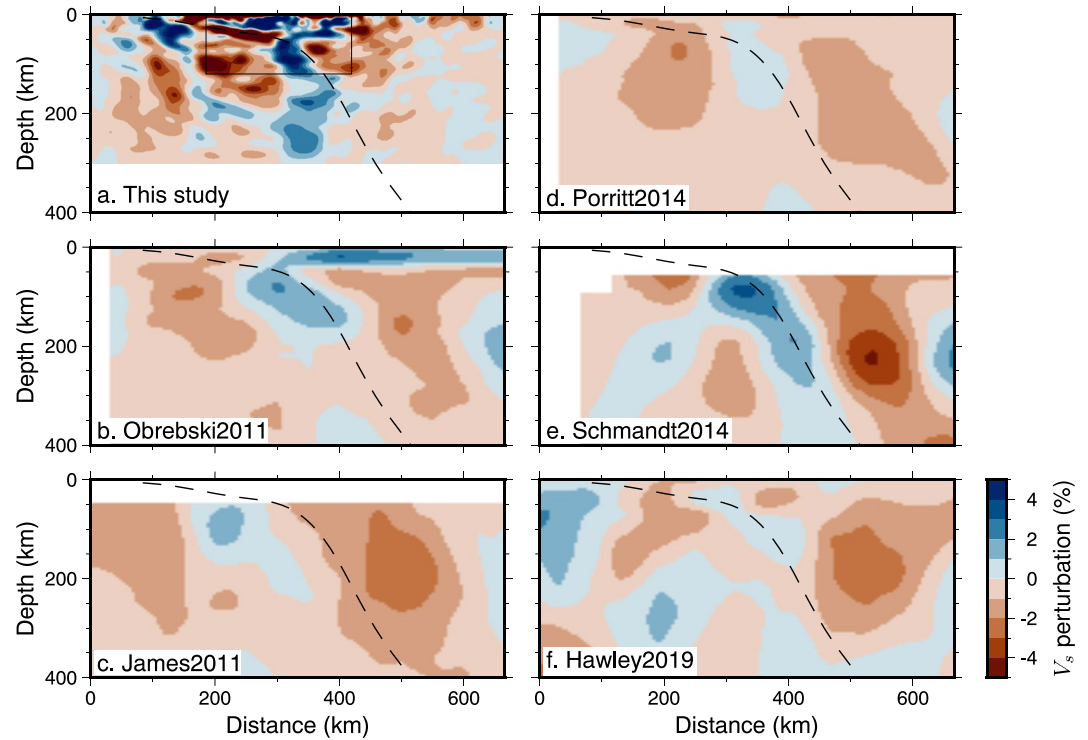


Figure 13. Vertical cross-sections showing V_S models along the CASC93 experiment transect (latitude of 44.44°N). The dashed line shows the slab contour of the JdF plate (Hayes et al., 2018). (a) FWI V_S model from this study. The rectangular box represents the region shown in Figure 7. (b) V_S model from DNA10 (Obrebski et al., 2011). (c) V_S model from NWUS11-S (James et al., 2011). (d) V_S model from DNA13 (Porritt et al., 2014). (e) V_S model from US-SL-2014 (Schmandt & Lin, 2014). (f) V_S model from Casc19-S (Hawley & Allen, 2019).

to the 600°C isotherm in Hyndman and Peacock (2003). As already noted by M. G. Bostock et al. (2002), this also suggests a significant temperature contrast between the forearc and the backarc mantle, which could explain the sharp eastward increase of heat flow measured at the surface (Blackwell et al., 1982). Serpentinization reactions also produce magnetite. Since the temperature in the forearc mantle wedge is expected to be cooler than 580°C (Hyndman & Peacock, 2003), the Curie temperature of magnetite, a magnetic anomaly is thus expected along the Cascadia forearc. Such a large anomaly is indeed observed, associated with a gravity low (Blakely et al., 2005) and thus the hypothesis of a highly hydrated mantle wedge is also supported by potential field anomalies.

Fluid pathways in the mantle wedge are still unclear, but tomographic studies suggest that fluids do not migrate vertically (e.g., Halpaap et al., 2018; Schurr et al., 2003). Instead, the fluids follow oblique diverging paths oriented toward the volcanic arc and/or upward the subduction interface toward the accretionary wedge, separated by a zone in the mantle wedge with low-fluid content. These intriguing observations were recently explained by numerical modeling of water migration in the mantle wedge with a two-phase flow approach (H. Wang et al., 2019). The water migration models in this study are characterized by the development of two water pathways with a low-porosity divide in between, which result from the bending of the overlying lithosphere that produces a zone of overpressure (which can reach up to 50% of the lithostatic pressure) and low-porosity in the mantle wedge. If we relate the decrease of density and seismic velocities observed in the serpentinized mantle wedge to the amount of mantle hydration, our FWI model clearly suggests two diverging fluid pathways with a core that has higher density and seismic velocities, located beneath the eastern margin of the

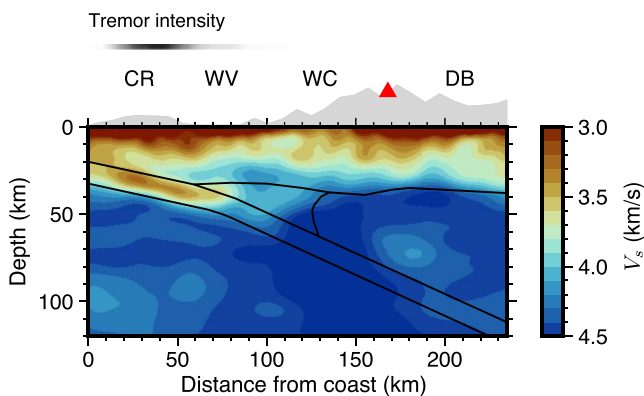


Figure 14. Comparison between our final V_S model and the main interfaces reconstructed by inversion of short period scattered teleseismic body waves (M. G. Bostock et al., 2002). The tremor intensity represents the number of tremors in every 2 km bin with a horizontal search radius of 20 km. Note the coincidence between the horizontal extent of the low-velocity zone and the occurrence of tremors.

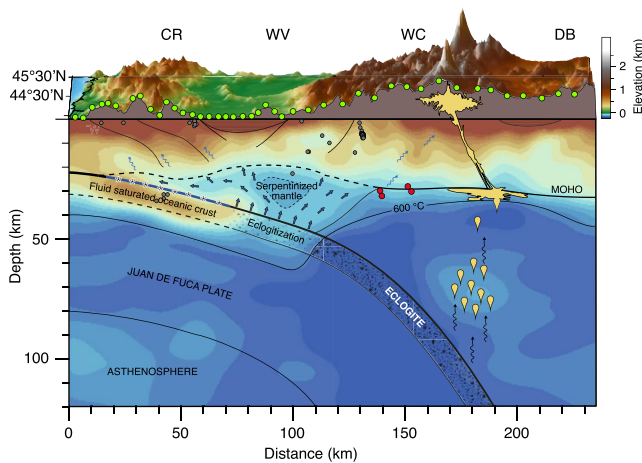


Figure 15. Interpretation of the V_S model shown in Figure 7, with (vertical exaggerated) topography plotted on top. The green circles show the positions of the stations of the CASC93 temporary experiment. The gray and red circles indicate the locations of crust earthquakes (Dunham & Kiser, 2020) and deep long-period events (Vidale et al., 2014), respectively. The thick black line draws the subduction interface that corresponds to the downgoing Juan de Fuca plate. Straight thick blue arrows indicate the path of ascending fluids originating from the slab that react with the olivine minerals of the mantle wedge to produce serpentinitized mantle with reduced density and seismic velocities. Wiggled thin blue arrows indicate the hypothesized paths followed by fluids in the forearc crust. The Moho beneath the forearc and the volcanic arc is defined from the 3.8 km/s isocontour in the V_S model. The 600°C isotherm taken from Hyndman and Peacock (2003) is indicated by a thin black line.

Willamette Valley. Magnetotelluric studies imaged conductive features that approximately correspond to these two hypothesized fluid pathways (Evans et al., 2014; Wannamaker et al., 2014). A first prominent conductive anomaly (resistivity $< 1 \Omega\text{-m}$) which diverges eastward, can be traced from the top of the slab to the Moho beneath the western Cascades, from where it extends horizontally further to the east. Interestingly, Vidale et al. (2014) reported deep long-period earthquakes (red circles in Figure 15) located ~ 40 km west of the volcanic arc, near the Moho, that is, coinciding with the horizontal part of the first conductivity anomaly. Deep long-period earthquakes are commonly observed beneath volcanoes, associated with the movement of fluids (Chouet & Matoza, 2013). The location beneath the western Cascades near the Moho thus gives further support to the hypothesis of fluids rising from the slab, percolating through the serpentinitized mantle wedge, and reaching the base of the forearc crust. The second conductive anomaly follows the plate interface updip and emerges offshore, at the front of the accretionary wedge.

Around 100 km depth, fluids released by dehydration of the slab reduce the solidus temperature and produce partial melting. The presence of melt will lower the shear velocity and, to a lower extent, the compressional velocity, and thus a positive V_p/V_S anomaly is a good indicator of partial melt. Our model indeed reveals an anomaly that possesses all the attributes of partial melt, beneath the volcanic arc at around 70 km depth, which could indeed be the deep source of the magma plumbing system. Magnetotelluric data are equivocal on whether there is a conductor that could be related to partial melt at this depth, because of the mask produced by the strong shallow conductive anomaly beneath the arc (Evans et al., 2014).

The forearc crust is characterized by an anomalously low V_p/V_S ratio, which can only be explained by large-scale silica enrichment (Brocher, 2005;

Chevrot & van der Hilst, 2000; Christensen, 1996). This enrichment requires massive transport of fluids saturated in silica that migrate upward through the forearc crust and precipitate when the solubility of silica drops because of the temperature decrease (Manning, 1994). Massive and pervasive mineralized quartz veins are indeed a well-documented ubiquitous feature of forearc crusts (e.g., Breeding & Ague, 2002; Halpaap et al., 2018; Ramachandran & Hyndman, 2012), which may have contributed to the silica enrichment of continents. These quartz veins often host gold deposits which result from extensive leaching of the crust by hot fluids (Kerrick, 1999).

5. Conclusions

We have imaged the deep architecture of the subduction beneath central Cascadia, from the surface to 300 km depth, by inverting complete P and SH teleseismic waveforms. Compared to classical tomographic studies, the teleseismic FWI approach simultaneously constrains density, V_p , V_S , and the V_p/V_S ratio with fine spatial resolution. The final tomographic models provide new insight into the dehydration of the subducted Juan de Fuca slab and the associated eclogitization metamorphic reactions. They also reveal the fluid pathways through the forearc mantle as well as a partial melt zone around 75 km depth beneath the volcanic arc.

The main limitations of this study stem from the linear geometry of the acquisition, and from the short duration of the CASC93 experiment. We thus expect that more detailed and robust tomographic images could be obtained in northern Cascadia, where the stations are both more numerous and better distributed. Another important perspective will be to extend full waveform inversion to general anisotropic media (Beller & Chevrot, 2020) to constrain the 3D distribution of seismic anisotropy in the Cascadia subduction zone.

Data Availability Statement

The teleseismic waveforms are publicly available from Incorporated Research Institutions for Seismology Data Management Center (IRIS DMC). The FDSN code of the CASC93 experiment is XZ (1993–1994). The FWI code is available upon request to the corresponding author, and it will be released to the public soon.

Acknowledgments

We thank Roy Hyndman and an anonymous reviewer for their insightful and constructive reviews. V. Monteiller was supported by the European Union's Horizon 2020 research and innovation programme under the ChESEE project, grant agreement No. 823844. This work was performed using HPC resources from GENCI-IDRIS (Grant 2021-101085) and CALMIP (Grant P20012). The authors also acknowledge PRACE for awarding us access to Marconi100 at CINECA, Italy.

References

- Aki, K., Christofferson, A., & Husebye, E. S. (1977). Determination of the three-dimensional seismic structures of the lithosphere. *Journal of Geophysical Research*, 82(2), 277–296. <https://doi.org/10.1029/jb082i002p00277>
- Audet, P., Bostock, M. G., Boyarko, D. C., Brudzinski, M. R., & Allen, R. M. (2010). Slab morphology in the Cascadia fore arc and its relation to episodic tremor and slip. *Journal of Geophysical Research*, 115, B00A16. <https://doi.org/10.1029/2008jb006053>
- Audet, P., Bostock, M. G., Christensen, N. I., & Peacock, S. M. (2009). Seismic evidence for overpressured subducted oceanic crust and megathrust fault sealing. *Nature*, 457(7225), 76–78. <https://doi.org/10.1038/nature07650>
- Audet, P., & Bürgmann, R. (2014). Possible control of subduction zone slow-earthquake periodicity by silica enrichment. *Nature*, 510(7505), 389–392. <https://doi.org/10.1038/nature13391>
- Beller, S., & Chevrot, S. (2020). Probing depth and lateral variations of upper-mantle seismic anisotropy from full-waveform inversion of teleseismic body-waves. *Geophysical Journal International*, 222(1), 352–387. <https://doi.org/10.1093/gji/ggaa069>
- Beller, S., Monteiller, V., Combe, L., Operto, S., & Nolet, G. (2018). On the sensitivity of teleseismic full-waveform inversion to Earth parametrization, initial model and acquisition design. *Geophysical Journal International*, 212(2), 1344–1368. <https://doi.org/10.1093/gji/ggx480>
- Beller, S., Monteiller, V., Operto, S., Nolet, G., Paul, A., & Zhao, L. (2018). Lithospheric architecture of the South-Western Alps revealed by multiparameter teleseismic full-waveform inversion. *Geophysical Journal International*, 212(2), 1369–1388. <https://doi.org/10.1093/gji/ggx216>
- Blackwell, D. D., Bowen, R. G., Hull, D. A., Riccio, J., & Steele, J. L. (1982). Heat flow, arc volcanism, and subduction in northern Oregon. *Journal of Geophysical Research*, 87(B10), 8735. <https://doi.org/10.1029/jb087ib10p08735>
- Blakely, R. J., Brocher, T. M., & Wells, R. E. (2005). Subduction-zone magnetic anomalies and implications for hydrated forearc mantle. *Geology*, 33(6), 445. <https://doi.org/10.1130/g21447.1>
- Bostock, M. (2013). The Moho in subduction zones. *Tectonophysics*, 609, 547–557. <https://doi.org/10.1016/j.tecto.2012.07.007>
- Bostock, M. G., Hyndman, R. D., Rondenay, S., & Peacock, S. M. (2002). An inverted continental Moho and serpentinization of the forearc mantle. *Nature*, 417(6888), 536–538. <https://doi.org/10.1038/417536a>
- Breeding, C. M., & Ague, J. J. (2002). Slab-derived fluids and quartz-vein formation in an accretionary prism, Otago Schist, New Zealand. *Geology*, 30(6), 499. [https://doi.org/10.1130/0091-7613\(2002\)030<0499:sdfaqv>2.0.co;2](https://doi.org/10.1130/0091-7613(2002)030<0499:sdfaqv>2.0.co;2)
- Brocher, T. (2005). Empirical relations between elastic wavespeeds and density in the Earth's crust. *Bulletin of the Seismological Society of America*, 95(6), 2081–2092. <https://doi.org/10.1785/0120050077>
- Chevrot, S., Sylvander, M., Villaseñor, A., Díaz, J., Stehly, L., Boué, P., et al. (2022). Passive imaging of collisional orogens: A review of a decade of geophysical studies in the Pyrénées. *BSGF - Earth Sciences Bulletin*, 193, 1. <https://doi.org/10.1051/bsgf/2021049>
- Chevrot, S., & van der Hilst, R. (2000). The Poisson ratio of the Australian crust: Geological and geophysical implications. *Earth and Planetary Science Letters*, 183(1–2), 121–132. [https://doi.org/10.1016/s0012-821x\(00\)00264-8](https://doi.org/10.1016/s0012-821x(00)00264-8)
- Chouet, B. A., & Matoza, R. S. (2013). A multi-decadal view of seismic methods for detecting precursors of magma movement and eruption. *Journal of Volcanology and Geothermal Research*, 252, 108–175. <https://doi.org/10.1016/j.jvolgeores.2012.11.013>
- Christensen, N. I. (1966). Elasticity of ultrabasic rocks. *Journal of Geophysical Research*, 71(24), 5921–5931. <https://doi.org/10.1029/jz071i024p05921>
- Christensen, N. I. (1996). Poisson's ratio and crustal seismology. *Journal of Geophysical Research*, 101(B2), 3139–3156. <https://doi.org/10.1029/95jb03446>
- Christensen, N. I. (2004). Serpentinites, peridotites, and seismology. *International Geology Review*, 49(9), 795–816. <https://doi.org/10.2747/0020-6814.46.9.795>
- Delph, J. R., Levander, A., & Niu, F. (2018). Fluid controls on the heterogeneous seismic characteristics of the Cascadia margin. *Geophysical Research Letters*, 45(20), 11021–11029. <https://doi.org/10.1029/2018gl079518>
- DeMets, C., Gordon, R. G., Argus, D. F., & Stein, S. (1990). Current plate motions. *Geophysical Journal International*, 101(2), 425–478. <https://doi.org/10.1111/j.1365-246x.1990.tb06579.x>
- Dunham, A., & Kiser, E. (2020). Local earthquake tomography of the central Oregon forearc using a large-N, short duration, nodal array. *Earth and Planetary Science Letters*, 551, 116559. <https://doi.org/10.1016/j.epsl.2020.116559>
- Evans, R. L., Wannamaker, P. E., McGary, R. S., & Elsenbeck, J. (2014). Electrical structure of the central Cascadia subduction zone: The EMSLAB Lincoln Line revisited. *Earth and Planetary Science Letters*, 402, 265–274. <https://doi.org/10.1016/j.epsl.2013.04.021>
- Favier, N., Chevrot, S., & Komatitsch, D. (2004). Near-field influences on shear wave splitting and traveltime sensitivity kernels. *Geophysical Journal International*, 156(3), 467–482. <https://doi.org/10.1111/j.1365-246x.2004.02178.x>
- Gerya, T. V., Fossati, D., Cantieni, C., & Seward, D. (2009). Dynamic effects of aseismic ridge subduction: Numerical modelling. *European Journal of Mineralogy*, 21(3), 649–661. <https://doi.org/10.1127/0935-1221/2009/0021-1931>
- Gosselin, J. M., Audet, P., Estève, C., McLellan, M., Mosher, S. G., & Schaeffer, A. J. (2020). Seismic evidence for megathrust fault-valve behavior during episodic tremor and slip. *Science Advances*, 6(4). <https://doi.org/10.1126/sciadv.aay5174>
- Guo, H., McGuire, J. J., & Zhang, H. (2021). Correlation of porosity variations and rheological transitions on the southern Cascadia megathrust. *Nature Geoscience*, 14(5), 341–348. <https://doi.org/10.1038/s41561-021-00740-1>
- Halpaap, F., Rondenay, S., & Ottemöller, L. (2018). Seismicity, deformation, and metamorphism in the Western Hellenic subduction zone: New constraints from tomography. *Journal of Geophysical Research: Solid Earth*, 123(4), 3000–3026. <https://doi.org/10.1002/2017jb015154>
- Hansen, R. T., Bostock, M. G., & Christensen, N. I. (2012). Nature of the low velocity zone in Cascadia from receiver function waveform inversion. *Earth and Planetary Science Letters*, 337–338, 25–38. <https://doi.org/10.1016/j.epsl.2012.05.031>
- Hawley, W. B., & Allen, R. M. (2019). The fragmented death of the Farallon plate. *Geophysical Research Letters*, 46(13), 7386–7394. (US Case19-S model). <https://doi.org/10.1029/2019gl083437>
- Hayes, G. P., Moore, G. L., Portner, D. E., Hearne, M., Flamme, H., Furtney, M., & Smoczyk, G. M. (2018). Slab2, a comprehensive subduction zone geometry model. *Science*, 362(6410), 58–61. <https://doi.org/10.1126/science.aat4723>
- Hyndman, R. D. (2013). Downdip landward limit of Cascadia great earthquake rupture. *Journal of Geophysical Research: Solid Earth*, 118(10), 5530–5549. <https://doi.org/10.1002/jgrb.50390>
- Hyndman, R. D., McCrory, P. A., Wech, A., Kao, H., & Ague, J. (2015). Cascadia subducting plate fluids channelled to fore-arc mantle corner: ETS and silica deposition. *Journal of Geophysical Research: Solid Earth*, 120(6), 4344–4358. <https://doi.org/10.1002/2015jb011920>
- Hyndman, R. D., & Peacock, S. M. (2003). Serpentinization of the forearc mantle. *Earth and Planetary Science Letters*, 212(3–4), 417–432. [https://doi.org/10.1016/s0012-821x\(03\)00263-2](https://doi.org/10.1016/s0012-821x(03)00263-2)
- James, D. E., Fouch, M. J., Carlson, R. W., & Roth, J. B. (2011). Slab fragmentation, edge flow and the origin of the Yellowstone hotspot track. *Earth and Planetary Science Letters*, 311(1–2), 124–135. <https://doi.org/10.1016/j.epsl.2011.09.007>

- Kan, L.-Y., Chevrot, S., & Monteiller, V. (2023). A consistent multiparameter Bayesian full waveform inversion scheme for imaging heterogeneous isotropic elastic media. *Geophysical Journal International*, 232(2), 864–883. <https://doi.org/10.1093/gji/ggac363>
- Kao, H., Shan, S.-J., Dragert, H., Rogers, G., Cassidy, J. F., & Ramachandran, K. (2005). A wide depth distribution of seismic tremors along the northern Cascadia margin. *Nature*, 436(7052), 841–844. <https://doi.org/10.1038/nature03903>
- Kennett, B. L. N., Engdahl, E. R., & Buland, R. (1995). Constraints on seismic velocities in the Earth from traveltimes. *Geophysical Journal International*, 122(1), 108–124. <https://doi.org/10.1111/j.1365-246x.1995.tb03540.x>
- Kerrick, R. (1999). Nature's gold factory. *Science*, 284(5423), 2101–2102. <https://doi.org/10.1126/science.284.5423.2101>
- Komatitsch, D., & Tromp, J. (1999). Introduction to the spectral-element method for 3-D seismic wave propagation. *Geophysical Journal International*, 139(3), 806–822. <https://doi.org/10.1046/j.1365-246x.1999.00967.x>
- Manning, C. E. (1994). The solubility of quartz in H₂O in the lower crust and upper mantle. *Geochimica et Cosmochimica Acta*, 58(22), 4831–4839. [https://doi.org/10.1016/0016-7037\(94\)90214-3](https://doi.org/10.1016/0016-7037(94)90214-3)
- McCrory, P. A., Blair, J. L., Waldhauser, F., & Oppenheimer, D. H. (2012). Juan de Fuca slab geometry and its relation to Wadati-Benioff zone seismicity. *Journal of Geophysical Research*, 117(B9), B09306. <https://doi.org/10.1029/2012jb009407>
- Monteiller, V., Beller, S., Plazolles, B., & Chevrot, S. (2021). On the validity of the planar wave approximation to compute synthetic seismograms of teleseismic body waves in a 3-D regional model. *Geophysical Journal International*, 224(3), 2060–2076. <https://doi.org/10.1093/gji/ggaa570>
- Monteiller, V., Chevrot, S., Komatitsch, D., & Fuji, N. (2013). A hybrid method to compute short-period synthetic seismograms of teleseismic body waves in a 3-D regional model. *Geophysical Journal International*, 192(1), 230–247. <https://doi.org/10.1093/gji/ggs006>
- Monteiller, V., Chevrot, S., Komatitsch, D., & Wang, Y. (2015). Three-dimensional full waveform inversion of short-period teleseismic wavefields based upon the SEM-DSM hybrid method. *Geophysical Journal International*, 202(2), 811–827. <https://doi.org/10.1093/gji/ggv189>
- Nabelek, J., Li, X., Azevedo, S., Braunmiller, J., Fabritius, A., Leitner, B., et al. (1993). A high-resolution image of the Cascadia subduction zone from teleseismic converted phases recorded by a broadband seismic array. *Eos Trans. AGU*, 74(43), 431.
- Nakajima, J., Matsuzawa, T., Hasegawa, A., & Zhao, D. (2001). Three-dimensional structure of v_p , v_s , and v_p/v_s beneath northeastern Japan: Implications for arc magmatism and fluids. *Journal of Geophysical Research*, 106(B10), 21843–21857. <https://doi.org/10.1029/2000jb000008>
- Nissen-Meyer, T., Driel, M., Stähler, S., Hosseini, K., Hempel, S., Auer, L., et al. (2014). AxiSEM: Broadband 3-D seismic wavefields in axisymmetric media. *Solid Earth*, 1, 425–445. <https://doi.org/10.5194/se-5-425-2014>
- Nocedal, J., & Wright, S. (2006). *Numerical optimization*. Springer.
- Obrebski, M., Allen, R. M., Pollitz, F., & Hung, S.-H. (2011). Lithosphere-asthenosphere interaction beneath the Western United States from the joint inversion of body-wave traveltimes and surface-wave phase velocities. *Geophysical Journal International*, 185(2), 1003–1021. <https://doi.org/10.1111/j.1365-246x.2011.04990.x>
- Obrebski, M., Allen, R. M., Xue, M., & Hung, S.-H. (2010). Slab-plume interaction beneath the Pacific northwest. *Geophysical Research Letters*, 37(14), L14305. <https://doi.org/10.1029/2010gl043489>
- Oleskevich, D. A., Hyndman, R. D., & Wang, K. (1999). The updip and downdip limits to great subduction earthquakes: Thermal and structural models of Cascadia, south Alaska, SW Japan, and Chile. *Journal of Geophysical Research*, 104(B7), 14965–14991. <https://doi.org/10.1029/1999jb900060>
- Oliver, D. S. (1998). Calculation of the inverse of the covariance. *Mathematical Geology*, 30(7), 911–933. <https://doi.org/10.1023/a:1021734811230>
- Peacock, S. A. (1990). Fluid processes in subduction zones. *Science*, 248(4953), 329–337. <https://doi.org/10.1126/science.248.4953.329>
- Peacock, S. M. (1993). Large-scale hydration of the lithosphere above subducting slabs. *Chemical Geology*, 108(1–4), 49–59. [https://doi.org/10.1016/0009-2541\(93\)90317-c](https://doi.org/10.1016/0009-2541(93)90317-c)
- Peacock, S. M., Christensen, N. I., Bostock, M. G., & Audet, P. (2011). High pore pressures and porosity at 35 km depth in the Cascadia subduction zone. *Geology*, 39(5), 471–474. <https://doi.org/10.1130/g31649.1>
- Peacock, S. M., & Hyndman, R. D. (1999). Hydrous minerals in the mantle wedge and the maximum depth of subduction thrust earthquakes. *Geophysical Research Letters*, 26(16), 2517–2520. <https://doi.org/10.1029/1999gl005558>
- Peacock, S. M., Rushmer, T., & Thompson, A. B. (1994). Partial melting of subducting oceanic crust. *Earth and Planetary Science Letters*, 121(1–2), 227–244. [https://doi.org/10.1016/0012-821x\(94\)90042-6](https://doi.org/10.1016/0012-821x(94)90042-6)
- Peacock, S. M., & Wang, K. (1999). Seismic consequences of warm versus cool subduction metamorphism: Examples from southwest and northeast Japan. *Science*, 286(5441), 937–939. <https://doi.org/10.1126/science.286.5441.937>
- Porritt, R. W., Allen, R. M., & Pollitz, F. F. (2014). Seismic imaging east of the Rocky Mountains with USArray. *Earth and Planetary Science Letters*, 402, 16–25. (US DNA13 model). <https://doi.org/10.1016/j.epsl.2013.10.034>
- Ramachandran, K., & Hyndman, R. D. (2012). The fate of fluids released from subducting slab in northern Cascadia. *Solid Earth*, 3(1), 121–129. <https://doi.org/10.5194/se-3-121-2012>
- Rogers, G., & Dragert, H. (2003). Episodic tremor and slip on the Cascadia subduction zone: The chatter of silent slip. *Science*, 300(5627), 1942–1943. <https://doi.org/10.1126/science.1084783>
- Rondenay, S., Bostock, M. G., & Shragge, J. (2001). Multiparameter two-dimensional inversion of scattered teleseismic body waves 3. Application to the Cascadia 1993 data set. *Journal of Geophysical Research*, 106(B12), 30795–30807. <https://doi.org/10.1029/2000jb000039>
- Savard, G., Bostock, M. G., & Christensen, N. I. (2018). Seismicity, metamorphism, and fluid evolution across the northern Cascadia fore arc. *Geochemistry, Geophysics, Geosystems*, 19(6), 1881–1897. <https://doi.org/10.1029/2017gc007417>
- Schmandt, B., & Humphreys, E. (2010). Complex subduction and small-scale convection revealed by body-wave tomography of the Western United States upper mantle. *Earth and Planetary Science Letters*, 297(3–4), 435–445. <https://doi.org/10.1016/j.epsl.2010.06.047>
- Schmandt, B., & Lin, F. (2014). P and S wave tomography of the mantle beneath the United States. *Geophysical Research Letters*, 41(18), 6342–6349. US US-SL-2014 model. <https://doi.org/10.1002/2014gl061231>
- Schurr, B., Asch, G., Rietbrock, A., Trumbull, R., & Haberland, C. (2003). Complex patterns of fluid and melt transport in the central Andean subduction zone revealed by attenuation tomography. *Earth and Planetary Science Letters*, 215(1–2), 105–119. [https://doi.org/10.1016/s0012-821x\(03\)00441-2](https://doi.org/10.1016/s0012-821x(03)00441-2)
- Tarantola (2005). *Inverse problem theory*. SIAM.
- Tauzin, B., Bodin, T., Debayle, E., Perrillat, J.-P., & Reynard, B. (2016). Multi-mode conversion imaging of the subducted Gorda and Juan de Fuca plates below the North American continent. *Earth and Planetary Science Letters*, 440, 135–146. <https://doi.org/10.1016/j.epsl.2016.01.036>
- Thomas, A. M., & Bostock, M. G. (2015). Identifying low-frequency earthquakes in central Cascadia using cross-station correlation. *Tectonophysics*, 658, 111–116. <https://doi.org/10.1016/j.tecto.2015.07.013>
- Trehu, A. M., Asudeh, I., Brocher, T. M., Luetgert, J. H., Mooney, W. D., Nabelek, J. L., & Nakamura, Y. (1994). Crustal architecture of the Cascadia forearc. *Science*, 266(5183), 237–243. <https://doi.org/10.1126/science.266.5183.237>

- Trinh, P., Brossier, R., Métivier, L., Virieux, J., & Wellington, P. (2017). Bessel smoothing filter for spectral-element mesh. *Geophysical Journal International*, 209(3), 1489–1512. <https://doi.org/10.1093/gji/ggx103>
- Tromp, J., Tape, C., & Liu, Q. Y. (2005). Seismic tomography, adjoint methods, time reversal and banana-doughnut kernels. *Geophysical Journal International*, 160(1), 195–216. <https://doi.org/10.1111/j.1365-246x.2004.02453.x>
- van Hunen, J., van den Berg, A. P., & Vlaar, N. J. (2002). On the role of subducting oceanic plateaus in the development of shallow flat subduction. *Tectonophysics*, 352(3–4), 317–333. [https://doi.org/10.1016/s0040-1951\(02\)00263-9](https://doi.org/10.1016/s0040-1951(02)00263-9)
- Vidale, J. E., Schmidt, D. A., Malone, S. D., Hotovec-Ellis, A. J., Moran, S. C., Creager, K. C., & Houston, H. (2014). Deep long-period earthquakes west of the volcanic arc in Oregon: Evidence of serpentine dehydration in the fore-arc mantle wedge. *Geophysical Research Letters*, 41(2), 370–376. <https://doi.org/10.1002/2013gl059118>
- Virieux, J., & Operto, S. (2009). An overview of full-waveform inversion in exploration geophysics. *Geophysics*, 74(6), WCC1–WCC26. <https://doi.org/10.1190/1.3238367>
- Wang, H., Huismans, R. S., & Rondenay, S. (2019). Water migration in the subduction mantle wedge: A two-phase flow approach. *Journal of Geophysical Research: Solid Earth*, 124(8), 9208–9225. <https://doi.org/10.1029/2018jb017097>
- Wang, K., Wang, Y., Song, X., Tong, P., Liu, Q., & Yang, Y. (2021). Full-waveform inversion of high-frequency teleseismic body waves based on multiple plane-wave incidence: Methods and practical applications. *Bulletin of the Seismological Society of America*, 112(1), 118–132. <https://doi.org/10.1785/0120210094>
- Wang, Y., Chevrot, S., Monteiller, V., Komatitsch, D., Mouthereau, F., Manatschal, G., et al. (2016). The deep roots of the Western Pyrenees revealed by full waveform inversion of teleseismic P waves. *Geology*, 44(6), 475–478. <https://doi.org/10.1130/g37812.1>
- Wannamaker, P. E., Evans, R. L., Bedrosian, P. A., Unsworth, M. J., Maris, V., & McGary, R. S. (2014). Segmentation of plate coupling, fate of subduction fluids, and modes of arc magmatism in Cascadia, inferred from magnetotelluric resistivity. *Geochemistry, Geophysics, Geosystems*, 15(11), 4230–4253. <https://doi.org/10.1002/2014gc005509>
- Watanabe, T. (1993). Effects of water and melt on seismic velocities and their application to characterization of seismic reflectors. *Geophysical Research Letters*, 20(24), 2933–2936. <https://doi.org/10.1029/93gl03170>
- Wech, A. G. (2021). Cataloging tectonic tremor energy radiation in the Cascadia subduction zone. *Journal of Geophysical Research: Solid Earth*, 126(10). <https://doi.org/10.1029/2021jb022523>
- Wech, A. G., & Creager, K. C. (2008). Automated detection and location of Cascadia tremor. *Geophysical Research Letters*, 35(20), L20302. <https://doi.org/10.1029/2008gl035458>
- Wells, R., Bukry, D., Friedman, R., Pyle, D., Duncan, R., Haeussler, P., & Wooden, J. (2014). Geologic history of Siletzia, a large igneous province in the Oregon and Washington coast range: Correlation to the geomagnetic polarity time scale and implications for a long-lived Yellowstone hotspot. *Geosphere*, 10(4), 692–719. <https://doi.org/10.1130/ges01018.1>
- Wilson, D. S. (1993). Confidence intervals for motion and deformation of the Juan de Fuca Plate. *Journal of Geophysical Research*, 98(B9), 16053. <https://doi.org/10.1029/93jb01227>